Monthly Notices of the ROYAL ASTRONOMICAL SOCIETY

MNRAS **544,** 1588–1607 (2025) https://doi.org/10.1093/mnras/staf1723
Advance Access publication 2025 October 9

CLASSY XII: nitrogen enrichment shaped by gas density and feedback

K. Z. Arellano-Córdova [1★] D. A. Berg [2] M. Mingozzi [3] B. L. James [3] F. Vincenzo [4] N. S. J. Rogers [5] E. D. Skillman [6] R. O. Amorín [7] F. Cullen [1] S. R. Flury [1] V. Abril-Melgarejo [3,8] J. Chisholm [2] T. Heckman,[9] M. J. Hayes [10] S. Hernandez [3] N. Kumari [3] C. Kobayashi [11] C. Leitherer,[3] C. L. Martin [12] Z. Martinez [2] T. Nanayakkara [13] K. S. Parker [2] P. Senchyna [14] C. Scarlata [6] M. G. Stephenson,[2] A. Wofford [15] X. Xu [5] and P. Zhu [16,17,18]

Affiliations are listed at the end of the paper

Accepted 2025 September 28. Received 2025 September 26; in original form 2025 July 15

ABSTRACT

We investigate the chemical evolution of N/O using a sample of 45 local star-forming galaxies from the CLASSY survey. This sample spans a wide range of galaxy properties, with robust determinations of nitrogen and oxygen abundances via the direct-T_e method. We explore how N/O relates to density structure, stellar mass, star formation rate (SFR), stellar age, compactness, and gas kinematics. In addition, we compare our results with those of galaxies at $z = 2$–10 where N/O ratios were derived from optical or UV nitrogen lines, aiming to identify chemical enrichment pathways across cosmic time. Our analysis shows that the N/O–O/H relation in CLASSY galaxies aligns with the trends seen in local galaxies and extragalactic H II regions, and that galaxies at $z = 2$–6 exhibit similar N/O values, indicating no significant redshift evolution in N/O for a fixed metallicity. We identify a significant correlation between electron density n_e([S II]) and N/O, suggesting that density structure contributes to the scatter in the N/O–O/H relation. The CLASSY galaxies with high SFRs or compact star formation show elevated N/O, though no strong correlation with stellar mass is found. We also find that high-velocity outflows ($v_{out} \gtrsim 350$ km s^{-1}) and low mass-loading factors are linked to elevated N/O, indicating that feedback plays a significant role. These results highlight the importance of density, star formation, and feedback from young stellar populations in shaping N/O enrichment and provide key insights for interpreting high-z galaxies observed with *James Webb Space Telescope*.

Key words: galaxies: abundances – galaxies: dwarf – galaxies: evolution – galaxies: ISM – galaxies: kinematics and dynamics.

1 INTRODUCTION

Understanding the star formation history of galaxies requires a detailed study of stellar mass assembly across redshifts. A fundamental probe of galaxy evolution is the chemical enrichment traced by the nucleosynthesis products of generations of stars, which provide insight into the mechanisms associated with the baryon cycle.

The abundances of carbon (C), nitrogen (N), and oxygen (O) relative to hydrogen (H) are among the most important tracers of the chemical enrichment in star-forming regions across cosmic time. O is produced over very short time-scales ($\sim$ 10 Myr) in massive stars and is subsequently ejected into the interstellar medium (ISM) by core-collapse supernovae (CCSNe). The oxygen abundance is commonly used as a proxy for the gas-phase metallicity. N is produced during the CNO cycle and is ejected into the ISM by both massive and intermediate-mass stars 4–7M$_\odot$ at a time-scale of ($\sim$ 250 Myr), and continues to be ejected over 1 Gyr. C is also produced by massive and low-mass stars (1 − 4M$_\odot$), and serves to catalyser for the production of N. (e.g. F. Matteucci & L. Greggio 1986; R. B. C. Henry, M. G. Edmunds & J. Köppen 2000; C. Kobayashi, A. I. Karakas & H. Umeda 2011; P. Ventura et al. 2013; F. Vincenzo et al. 2016; A. L. Schaefer et al. 2020; J. W. Johnson et al. 2023; F. Rizzuti et al. 2025). These elements are released on different time-scales through SN explosions and violent stellar winds, expelling C, N, and O into the ISM, where they become subject to the complex processes of the baryon cycle. For example, inflows of pristine gas dilute the metallicity and fuel new star formation, while outflows and gas recycling remove or redistribute metals (e.g. J. Tumlinson et al. 2017).

In this context, the different production time-scales of nitrogen and oxygen make it possible to build the N/O–O/H relation, which is an essential diagnostic of star formation and chemical enrichment histories of galaxies. The shape of the N/O–O/H relation mainly reflects the primary and secondary origins of N, determined by initial C production through triple-α burning and by pre-existing C from the CNO cycle, respectively. At metallicities ($12 + \log(O/H) \lesssim 8$), the chemical enrichment of N/O remains constant with O/H (plateau) indicating that N is evolving in lockstep with O, which is associated with the only contribution of massive stars. As metallicity increases, the AGB stars eject N into the ISM, increasing the N/O ratio (e.g. R. B. C. Henry et al. 2000; A. Nava et al. 2006; E. Pérez-Montero & T. Contini 2009; C. Kobayashi et al. 2011; F. Vincenzo et al. 2016;

★ E-mail: ziboney@gmail.com, k.arellano@ed.ac.uk

C. Kobayashi, A. I. Karakas & M. Lugaro 2020; J. W. Johnson et al. 2023).

In addition to the nucleosynthesis pathways of N and O, there are other physical mechanisms that shape the N/O–O/H ratio. For example, such a scatter might be related to differences in star formation histories, and low star formation efficiency (SFE) that reduces the production of oxygen while the production of N still continues from more evolved stars, and the chemical enrichment of N via the strong winds of Wolf–Rayet (WR) stars. Another important scenario that might contribute to the scatter in the N/O–O/H relation is mechanical feedback from massive stars, which can transport metals from stellar production sites out into the ISM (e.g. J. Chisholm, C. Tremonti & C. Leitherer 2018). At low metallicity, SNe can be suppressed below the typically assumed threshold (e.g. M. C. Jecmen & M. S. Oey 2023), which in turn can stunt the production of O via CCSNe. The lower O yields from such low-metallicity stellar populations would result in a net increase in N/O. Additionally, gas inflows can also play an important role in the N/O ratios, since inflows of pristine gas dilute the metallicity without altering nitrogen, and hence increase N/O (e.g. M. G. Edmunds 2001; J. Köppen & G. Hensler 2005; R. O. Amorín, E. Pérez-Montero & J. M. Vílchez 2010; B. Pérez-Díaz et al. 2024; C. Kobayashi & A. Ferrara 2024).

Local star-forming galaxies (SFGs) and extragalactic H II regions are a key laboratory for demonstrating which physical mechanisms and conditions drive the chemical abundance patterns of N and O across cosmic time. In this context, local SFGs offer an opportunity to study the chemical enrichment of N and O in much detail to disentangle the different gas conditions and galaxy properties that might contribute to the observed scatter N/O–O/H relation and that cannot be explained by the standard nucleosynthesis pathways of N/O.

In principle, the total abundance of an element is the contribution of each ionic species relative to hydrogen (e.g. N^+/H^+, N^{2+}/H^+, and N^{3+}/H^+), and its contribution will depend on the ionization state of the gas as well as the physical conditions of the ionized gas. The low-ionization lines of [N II] λλ6548,84 are the only collisional excited lines of N available in the optical, with a more that 40 per cent in their ionic abundance fraction of N^+/N contributing to the total N/H in low-ionization objects (e.g. A. Amayo, G. Delgado-Inglada & G. Stasińska 2021; D. A. Berg et al. 2021; Z. Martinez et al. 2025). In optical, the N/O abundance ratio is derived mostly using the [N II] λλ6548,84 and [O II] λλ3726,29 lines (or if available [O II] λλ7320,7330 but these lines are less commonly used) in H II regions and SFGS (e.g. R. B. C. Henry, A. Nava & J. X. Prochaska 2006; E. Pérez-Montero & T. Contini 2009; D. A. Berg et al. 2012; E. Pérez-Montero et al. 2013; K. V. Croxall et al. 2016; K. Z. Arellano-Córdova & M. Rodríguez 2020; M. G. Stephenson et al. 2023). If T_e is not available, N/O can also be estimated using strong-line methods, such as the [N II]/[O II] and [N II]/[S II] ratios (E. Pérez-Montero et al. 2013; E. Florido, A. Zurita & E. Pérez-Montero 2022; C. Hayden-Pawson et al. 2022).

With the several detections of UV N lines, N III] λλ1750, and N IV] λ1485 by the *James Webb Space Telescope (JWST)*, the higher ionization states of nitrogen can also be traced in high-z SFGs, allowing the opportunity to analyse the gas properties and chemical enrichment of N. Overall, measurements of N/O at high-z suggest that a significant portion of galaxy populations at these redshifts is characterized by extremely large N/O at low metallicity (e.g. A. J. Bunker et al. 2023; A. J. Cameron et al. 2023; Y. Isobe et al. 2023; M. Castellano et al. 2024; R. Marques-Chaves et al. 2024; D. Schaerer et al. 2024; M. Curti et al. 2025; M. J. Hayes et al. 2025). This elevated N/O might be explained by different scenarios such as the presence of massive stars or very massive stars, variations of the initial mass function (IMF), chemical enrichment of N/O via WR stars, gas heating by shocks, and the presence of active galactic nuclei (e.g. C. Charbonnel et al. 2023; J. S. Vink 2023; R. Maiolino et al. 2024; P. Senchyna et al. 2024; K. Watanabe et al. 2024; S. R. Flury et al. 2025b). Recent studies reveal that globular clusters share the same N/O enrichment observed in high-z galaxies, where dense environments enabled the formation of very massive stars, pointing to a possible common origin in the early universe (e.g. P. Senchyna et al. 2024; X. Ji et al. 2025). Alternatively, studies using chemical evolution modelling concluded that high UV N/O can be explained via different episodes of star formation following a quiescent phase (C. Kobayashi & A. Ferrara 2024). However, it is still unclear what is the impact in the abundances interpretation of using UV high-ionization lines and optical low-ionization lines tracing the N/O abundances.

In this work, we investigate the enrichment pathways of nitrogen and oxygen in the N/O–O/H relation by using 45 local SFGs from the COS Legacy Archive Spectroscopic SurveY (CLASSY) (e.g. D. A. Berg et al. 2022; B. L. James et al. 2022). The CLASSY galaxies have well-constrained direct abundances, total stellar masses ($M_\star$), star formation rates (SFRs), and gas physical and chemical properties derived from UV and optical data (e.g. D. A. Berg et al. 2022; B. L. James et al. 2022; M. Mingozzi et al. 2022; X. Xu et al. 2022). Our sample of local SFGs mimics the physical properties of high-z galaxies, particularly due to their high specific star formation rates (sSFR). Therefore, the wide range of physical properties in CLASSY enables us to study how these galaxy properties impact the observed N/O and N/H ratios. In particular, since most CLASSY galaxies are undergoing strong star formation, we can trace variations in N/O across different metallicities. With these results at $z \sim 0$, we can shed light on the chemical enrichment that shapes the N/O–O/H relation at all metallicities by addressing what properties are implied on the observed scatter at $z \sim 0$, and if such scenarios might be extended to high z.

The structure of the paper is as follows: In Section 2, we present the CLASSY galaxies and the archival properties analysed here, and an additional high-redshift sample gathered from the literature for comparison with our results. Section 3 describes the methodology used to derive the physical conditions and chemical abundances of N and O of this study. In Section 4, we present the N/O–O/H and N/H–O/H relations for CLASSY. We analyse the role of electron density, SFR, and kinematics in the observed scatter in the N/O–O/H relation. In these sections, we also compare our results with those of the high-z galaxies, and we present the results of the SFR and stellar mass surface densities for the CLASSY sample. Moreover, we introduce new chemical evolution models to explore the scatter of the N/O–O/H relation at low metallicities. The discussion of our results and the comparison of N/O across redshifts in Section 5. Finally, Section 6 summarizes our conclusions.

In this paper, we use the following solar abundance ratios taken from M. Asplund, A. M. Amarsi & N. Grevesse (2021): $12 + \log(O/H) = 8.69 \pm 0.04$ and $12 + \log(N/H) = 7.83 \pm 0.07$. We adopt a flat Lambda cold dark matter cosmology with $\Omega_m = 0.3$, $\Omega_\Lambda = 0.7$, and $H_0 = 70\,\mathrm{km\,s^{-1}\,Mpc^{-1}}$.

2 SAMPLE

2.1 CLASSY ($z \sim 0$)

Our sample comprises 45 optical spectra of SFGs ($0.002 < z < 0.182$) mainly gathered from the Sloan Digital Sky Survey (SDSS; K. N. Abazajian et al. 2009), with six objects from other facilities

such as the Large Binocular Telescope (LBT)/MODS, and the Very Large Telescope/MUSE/VIMOS. These observations are part of the CLASSY treasury survey D. A. Berg et al. (2022). A general overview of CLASSY can be found in D. A. Berg et al. (2022) and B. L. James et al. (2022), while the galaxy properties are reported in D. A. Berg et al. (2022), M. Mingozzi et al. (2022), and X. Xu et al. (2022). Overall, CLASSY covers a broad range of physical properties in terms of stellar mass, SFR, metallicity, and ionization parameter. However, note that CLASSY is biased towards UV-bright ($m_{\rm FUV} < 21$ AB arcsec^{-2}) and high SFR with the goal of mimicking high$-z$ galaxies. In K. Z. Arellano-Córdova et al. (2024, hereafter AC24a), we presented a study of the chemical abundance patterns of Ne, S, Cl, and Ar with O. Here, we continue that study by analysing the N abundances. We follow the methodology described in AC24a, which we summarize in Section 3.

2.2 Compilation of galaxy properties

Additionally, we used previous results from CLASSY to investigate the relationship between N/O and various gas and galaxy properties across different scaling relations. In particular, we considered the colour excess ($E(B-V)$), stellar mass, SFR, and optical sizes from D. A. Berg et al. (2022). The $E(B-V)$ values were derived from the Balmer decrement ratios, using the extinction law of J. A. Cardelli, G. C. Clayton & J. S. Mathis (1989). These $E(B-V)$ values were applied to correct the observed fluxes of different ions for dust attenuation, as reported by M. Mingozzi et al. (2022). We also collected the equivalent width (EW) of Hβ from M. Mingozzi et al. (2022).

For this study, we selected the set of galaxy properties that characterize the entire galaxy (see D. A. Berg et al. 2022, for details). The stellar masses and SFRs were derived from spectral energy distribution fitting, assuming a constant star formation history and a G. Chabrier (2003) IMF. The optical sizes of the galaxies (half-light radius, r_{50}) were measured using imaging in various bands, such as SDSS and Pan-STARRS, as reported in D. A. Berg et al. (2022, see their table 6). Finally, we also analysed the impact of stellar population age on the N/O results. We compiled stellar ages for the CLASSY sample from Parker et al., submitted, inferred using the method of J. Chisholm et al. (2019). This method consists of modelling the UV stellar continuum with a single-age stellar population from STARBURST99 (C. Leitherer et al. 1999), assuming a Kroupa IMF (see J. Chisholm et al. 2019, and Parker et al., submitted).

2.3 Archival sample at high z

In this analysis, we have incorporated the N/O and O/H data from the sample of H II regions and local SFGs extracted from the literature and presented in K. Z. Arellano-Córdova et al. (2024). This sample corresponds to the work of Y. I. Izotov et al. (2006), Y. I. Izotov et al. (2017), B. L. James et al. (2015), D. A. Berg et al. (2019), Y. I. Izotov, T. X. Thuan & N. G. Guseva (2021), and N. S. J. Rogers et al. (2022). We have also added the sample of Lyman-break galaxies from M. Loaiza-Agudelo, R. A. Overzier & T. M. Heckman (2020, $z < 0.2$), whose chemical properties were recalculated here using the dereddened fluxes reported by the authors.

We have compiled a sample of 22 galaxies at $z = 2$–10 with direct abundance determination where N/O is derived using either optical or UV N emission lines. This high-redshift sample with N/O from the optical lines includes two galaxies at $z \sim 2$ from R. L. Sanders et al. (2023a), The Sunburst Arc at $z = 2.37$ from B. Welch et al. (2025), Q2343-D40 from N. S. J. Rogers et al. (2024) at $z = 2.96$, two $z \sim 5$ EXCELS galaxies from K. Z. Arellano-Córdova et al. (2025), and 10 EXCELS galaxies from D. Scholte et al. (2025) and T. M. Stanton et al. (2025). For the sample with N/O derived using UV lines (e.g. [N IV] and N III]), we consider $z > 6$ galaxies from M. W. Topping et al. (2024b, RXCJ2248-ID, $z = 6.11$), Y. Isobe et al. (2023, GLASS_15008, $z = 6.23$), M. W. Topping et al. (2025a, A1703-zd6, $z = 7.04$), R. Marques-Chaves et al. (2024, CEERS_1019, $z = 8.63$), D. Schaerer et al. (2024, GN-z9p4, $z = 9.38$), and M. Curti et al. (2025, GS-z9-0, $z = 9.43$). We have distinguished the high-redshift sources according to the N emission lines used for calculating N/O. In the following figures of this study, the SFGs that use optical [N II] λ6584 to derive N/O are represented by pentagons, while the sample that uses UV [N IV] or N III] to derive N/O is represented by squares. It is worth mentioning that $z > 6$ objects may have a different nature compared to the CLASSY galaxies, as they are extremely compact clumps. However, we decided to include them in order to show the parameter space they occupy in the N/O–O/H relation and in other scaling relations presented in this study.

3 PHYSICAL CONDITIONS AND CHEMICAL ABUNDANCES

3.1 Electron density and temperature

For our analysis of N and O, we assumed the same electron temperature ($T_{\rm e}$) and density (n_e) structure for each galaxy presented in AC24a. These authors calculated electron densities using the [S II] λ6731/λ6717 density diagnostic and a three-zone temperature diagnostic, tracing the low ($T_{\rm e}$[O II]), intermediate ($T_{\rm e}$[S III]), and high ($T_{\rm e}$[O III]) ionization emitting regions of the gas. These temperatures were derived using the following diagnostics: [O II] ($\lambda\lambda$3726,3729)/($\lambda\lambda$7319,7320 $\lambda\lambda$7330,7331),[1] [N II] ($\lambda\lambda$6548,6584)/λ5755, [S III] $\lambda\lambda$9069,9532)/λ6312, and [O III] ($\lambda\lambda$4959,5007)/λ4363, respectively. The calculations of the electron density and temperature were done using the nebular analysis package PyNeb (V. Luridiana, C. Morisset & R. A. Shaw 2015, version 1.1.14) and the atomic data reported in Table 1.

3.2 Ionic and total abundances of N and O

To derive accurate ionic abundances, it is important to consider the appropriate $T_{\rm e}$ structure of each ionic species based on the ionization potential. J. E. Méndez-Delgado et al. (2023a) showed that the use of $T_{\rm e}$[O II] can overestimate the ionic abundances, since $T_{\rm e}$[O II] strongly depends on the electron density. To evaluate the impact of using $T_{\rm e}$[N II] and $T_{\rm e}$[O II] in calculating the N^+/O^+ ratio, we have selected 13 SFGs from CLASSY with measurements of both $T_{\rm e}$[N II] and $T_{\rm e}$[O II]. The electron density for these galaxies ranges from 100 to 480 cm^{-3} (for comparison between $T_{\rm e}$[O II] and $T_{\rm e}$[N II] see fig. 8 in AC24a)

In Fig. 1, we present the results of the N/O derived using $T_{\rm e}$[O II] and $T_{\rm e}$[N II]. For these 13 CLASSY galaxies, both results are consistent within the uncertainties, with differences <0.2 dex. The figure also illustrates that galaxies with high densities tend to have higher values of N/O. We discuss this in more detail in Section 4.3. We note that the N/O ratios using $T_{\rm e}$[N II] are more uncertain due to the faintness of the $T_{\rm e}$-sensitive [N II] λ5755. A

[1] Hereafter referred to as [O II] λ3727 and [O II] $\lambda\lambda$7320,7330 since these lines are blended due to the spectral resolution of the sample.

Table 1. Atomic data used in this work.

Ion	Transition probabilities (A_{ij})	Collision strengths (Υ_{ij})
O^+	C. Froese Fischer & G. Tachiev (2004)	R. Kisielius et al. (2009)
O^{2+}	C. Froese Fischer & G. Tachiev (2004)	K. M. Aggarwal & F. P. Keenan (1999)
N^+	C. Froese Fischer & G. Tachiev (2004)	S. S. Tayal (2011)
S^+	L. I. Podobedova, D. E. Kelleher & W. L. Wiese (2009)	S. S. Tayal & O. Zatsarinny (2010)
S^{2+}	L. I. Podobedova et al. (2009)	M. F. R. Grieve et al. (2014)

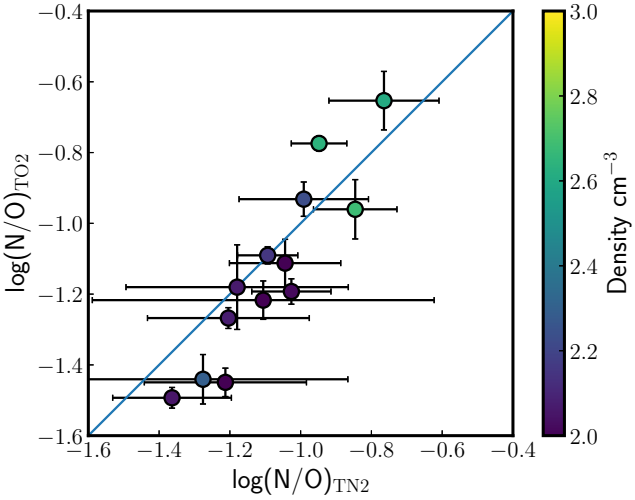

Figure 1. Comparison between log(N/O) derived using T_e[O II] and log(N/O) derived using T_e[N II], labelled as TO2 and TN2, respectively. The solid line represents the 1:1 relation, and the results are colour-coded with log(n_e[S II]). Note that the uncertainties in the measurements of log(N/O) are larger when using T_e[N II] compared to T_e[O II]. It shows that the two values are consistent within the uncertainties, with a slight offset towards lower values of log(N/O) at low $n_e$when using T_e[N II].

larger sample of ionized objects with both T_e[O II] and T_e[N II] is needed to corroborate the results in Fig. 1. Since T_e[O II] depends on density, and given the limited sample of galaxies with T_e[N II] measurements, we derive the ionic abundances of O^+ and N^+ using an estimated T_e from T_e[O III], based on the temperature relations of D. R. Garnett (1992) (see also E. Pérez-Montero et al. 2013; K. Z. Arellano-Córdova & M. Rodríguez 2020). For galaxies with only one measurement of T_e[O II] or T_e[N II] and without T_e[O III], we use those temperatures to estimate the low-ionization ionic abundances of N and O.

For the high-ionization ion O^{++}, we use T_e[O III] in 33 galaxies. For the remaining 10 galaxies, we use either T_e[S III] or T_e[O II] to estimate the high-ionization T_e, employing the temperature relations from D. R. Garnett (1992) and N. S. J. Rogers et al. (2021). The results of the temperature structure are consistent with those reported by AC24a (see their table 5). Therefore, with the two different ionic species of O available, we infer the metallicity of the CLASSY galaxies by adding the contributions from O^+/H^+ and O^{2+}/H^+.

To calculate the total abundances of N/O and N/H, we use ionization correction factors (ICFs) to account for unobserved transitions of different ionization species. ICFs are particularly important because they are one of the major sources of uncertainty in chemical abundance determinations. Following AC24a, we analysed different ICFs to select the most appropriate for this analysis. We derived N/O abundances using the ICF proposed by M. Peimbert & R. Costero (1969), $N^+/O^+ \approx$ N/O, based on the similar ionization potentials of O^+ and N^+. This ICF is widely used in H II regions and SFGs (e.g. K. V. Croxall et al. 2016; K. Z. Arellano-Córdova et al. 2020; D. A. Berg et al. 2020; C. Esteban et al. 2020; M. G. Stephenson et al. 2023).

Since the ICF of M. Peimbert & R. Costero (1969) is often chosen for N/O studies in the literature, we compare it with the ICFs from Y. I. Izotov et al. (2006) and A. Amayo et al. (2021), which depend on the ionization parameter defined as $O^{2+}/(O^+ + O^{2+})$. We find consistent results between the ICFs of M. Peimbert & R. Costero (1969) and Y. I. Izotov et al. (2006), with mean differences of 0.003 dex and a standard deviation of $\sigma = 0.04$ dex. However, the ICF of A. Amayo et al. (2021) shows a systematic shift to higher values of N/O with respect to the ICFs of Y. I. Izotov et al. (2006) and M. Peimbert & R. Costero (1969), but has a significantly lower dispersion than the others. The differences in N/O between A. Amayo et al. (2021) and M. Peimbert & R. Costero (1969) have means and standard deviations of 0.07 and 0.11 dex, respectively. We have adopted the ICF of M. Peimbert & R. Costero (1969) to provide the N/O and N/H abundances for CLASSY. The results of the ionic and total abundances for the N/H and N/O ratios are reported in Table 2.

4 RESULTS

4.1 The N/O versus O/H relation

In Fig. 2, we present the N/O ratio as a function of metallicity for CLASSY. Overall, we show that CLASSY galaxies follow a constant behaviour between N/O and metallicity. On the other hand, the CLASSY galaxies follow the plateau defined by dwarf SFGs (small circles) due to the primary contribution of nitrogen attributed mainly to massive stars. For higher metallicities, the CLASSY sample also shows high values of N/O at a fixed metallicity, consistent with the sample compiled from the literature from dwarf galaxies and H II regions (see also K. Z. Arellano-Córdova et al. 2024). In particular, at 12 + log(O/H) $\sim$ 8, CLASSY shows a large variation of the log(N/O) of up to 1.5 dex. We additionally highlight the seven galaxies exhibiting WR features with yellow stars. Four of them show broad He II λ4686 emission lines in the optical CLASSY spectra, with full width at half maximum (FWHM) $\gtrsim$ 500 km s^{-1}. The other three have WR features confirmed in previous studies (e.g. B. L. James et al. 2009; D. Miralles-Caballero et al. 2016; A. Paswan et al. 2019) (see Table 2). As shown in Fig. 2, the CLASSY galaxies with WR features tend to be located at high metallicities (12 + log(O/H) > 8.0) and low log(N/O) values (< −1.30) following the bulk of the observations, with the exception of J0127−0619 and J0823+2806, which shows slightly high N/O ratio than the rest of the sample hosting WR stars (Mrk 996; B. L. James et al. 2009). However, note that these WR galaxies are also consistent with the N/O ratios of local SFGs and H II regions for a fixed metallicity. In Fig. 2, we have incorporated a sample of high-redshift galaxies in comparison with CLASSY. Starting from the optical N/O results, we can see that the CLASSY galaxies cover the parameter spaces of $z = 2 - 6$ galaxies.

Table 2. Electron densities (n_e[S II] and n_e[Ar IV]), total oxygen abundance, and total nitrogen abundance for CLASSY galaxies are listed in columns 2–6. Stellar mass surface density and SFR surface density are reported in columns 7 and 8 (see Section 4.4.3). Column 9 indicates references for CLASSY galaxies previously identified with WR features. SFGs showing He II λ4686 emission with FWHM $\gtrsim$500 km s^{-1} are considered WR candidates.

Galaxy	n_e [S II] (cm^{-3})	n_e [Ar IV]† (cm^{-3})	12 + log(O/H)	log(N/O)	12 + log(N/H)	log(Σ_{SFR}) (M$_\odot$ yr^{-1} kpc^{-2})	log($\Sigma_\star$) (M$_\odot$ kpc^{-2})	WR Ref.
J0021+0052	< 100	–	8.15 ± 0.09	-1.20 ± 0.23	6.95 ± 0.14	$-0.04^{+0.14}_{-0.11}$	$1.98^{+0.18}_{-0.38}$	–
J0036−3333	< 100	–	8.16 ± 0.06	-0.96 ± 0.11	7.20 ± 0.09	$0.06^{+0.19}_{-0.21}$	$2.19^{+0.26}_{-0.23}$	–
J0127−0619	408 ± 40	–	8.13 ± 0.05	-0.88 ± 0.23	7.25 ± 0.13	$-0.39^{+0.15}_{-0.13}$	$3.10^{+0.18}_{-0.15}$	1
J0144+0453	< 100	–	7.45 ± 0.08	-1.61 ± 0.25	5.83 ± 0.22	$-0.58^{+0.29}_{-0.46}$	$1.88^{+0.24}_{-0.29}$	–
J0337−0502	180 ± 10	930 ± 150	7.23 ± 0.01	-1.32 ± 0.08	5.91 ± 0.06	$-0.31^{+0.07}_{-0.11}$	$1.07^{+0.24}_{-0.21}$	–
J0405−3648	< 100	–	7.28 ± 0.07	-1.30 ± 0.19	5.98 ± 0.15	$-1.24^{+0.31}_{-0.27}$	$1.18^{+0.28}_{-0.28}$	–
J0808+3948	1179 ± 100	6310 ± 3600	8.77 ± 0.05	-0.76 ± 0.06	7.92 ± 0.08	$-0.09^{+0.18}_{-0.25}$	$1.77^{+0.30}_{-0.17}$	–
J0823+2806	144 ± 24	5100 ± 4300	8.25 ± 0.10	-1.08 ± 0.26	7.16 ± 0.16	$0.09^{+0.15}_{-0.32}$	$1.99^{+0.33}_{-0.19}$	2
J0926+4427	< 100	–	7.97 ± 0.06	-1.83 ± 0.19	6.14 ± 0.14	$-0.63^{+0.13}_{-0.13}$	$1.10^{+0.30}_{-0.26}$	–
J0934+5514	100	8240 ± 4310	7.09 ± 0.02	–	–	$-0.58^{+0.09}_{-0.07}$	$1.21^{+0.15}_{-0.20}$	–
J0938+5428	106 ± 37	–	8.26 ± 0.08	-1.24 ± 0.22	7.02 ± 0.15	$-0.37^{+0.20}_{-0.17}$	$1.73^{+0.18}_{-0.29}$	–
J0940+2935	< 100	–	7.98 ± 0.23	-1.75 ± 0.36	6.23 ± 0.20	$-1.31^{+0.42}_{-0.37}$	$1.41^{+0.23}_{-0.40}$	–
J0942+3547	< 100	–	8.01 ± 0.07	-1.20 ± 0.28	6.81 ± 0.16	$-0.78^{+0.19}_{-0.12}$	$1.54^{+0.21}_{-0.29}$	–
J0944+3442	113 ± 48	–	7.66 ± 0.15	-0.99 ± 0.32	6.67 ± 0.19	$-0.35^{+0.19}_{-0.16}$	$1.26^{+0.44}_{-0.25}$	–
J0944−0038	138 ± 56	1060 ± 590	7.83 ± 0.02	-1.14 ± 0.19	6.69 ± 0.11	$-0.01^{+0.28}_{-0.65}$	$2.19^{+0.40}_{-0.23}$	–
J1016+3754	< 100	–	7.57 ± 0.03	-1.37 ± 0.22	6.19 ± 0.14	$-0.30^{+0.18}_{-0.18}$	$1.59^{+0.27}_{-0.22}$	–
J1024+0524	< 100	–	7.80 ± 0.05	-1.40 ± 0.22	6.41 ± 0.13	$-0.47^{+0.14}_{-0.12}$	$1.21^{+0.37}_{-0.24}$	–
J1025+3622	198 ± 56	–	8.13 ± 0.08	-1.36 ± 0.23	6.77 ± 0.14	$-0.32^{+0.14}_{-0.18}$	$1.51^{+0.25}_{-0.27}$	–
J1044+0353	267 ± 19	404 ± 110	7.55 ± 0.02	-1.48 ± 0.23	6.07 ± 0.14	$-0.39^{+0.11}_{-0.14}$	$1.00^{+0.41}_{-0.26}$	–
J1105+4444	113 ± 56	3160 ± 2600	8.23 ± 0.07	-1.46 ± 0.22	6.77 ± 0.15	$-0.23^{+0.28}_{-0.22}$	$2.06^{+0.29}_{-0.24}$	–
J1112+5503	407 ± 19	–	8.02 ± 0.04	-0.65 ± 0.07	7.36 ± 0.06	$0.14^{+0.20}_{-0.25}$	$2.13^{+0.33}_{-0.19}$	–
J1119+5130	< 100	–	7.59 ± 0.08	-1.59 ± 0.25	5.99 ± 0.16	$-0.85^{+0.21}_{-0.12}$	$1.50^{+0.15}_{-0.28}$	–
J1129+2034	< 100	–	8.30 ± 0.12	-1.48 ± 0.32	6.82 ± 0.19	$-0.12^{+0.38}_{-0.56}$	$2.34^{+0.37}_{-0.27}$	2
J1132+1411	< 100	–	8.24 ± 0.07	-1.45 ± 0.24	6.79 ± 0.15	$-0.17^{+0.24}_{-0.27}$	$2.07^{+0.28}_{-0.19}$	–
J1132+5722	122 ± 41	–	7.34 ± 0.09	-1.43 ± 0.21	5.91 ± 0.15	$-1.63^{+0.27}_{-0.35}$	$0.75^{+0.23}_{-0.26}$	–
J1144+4012	109 ± 48	–	8.65 ± 0.08	-1.20 ± 0.13	7.45 ± 0.12	$-0.13^{+0.20}_{-0.29}$	$2.25^{+0.18}_{-0.29}$	–
J1148+2546	113 ± 10	1190 ± 1070	8.01 ± 0.04	-1.39 ± 0.21	6.62 ± 0.14	$-0.02^{+0.17}_{-0.14}$	$1.59^{+0.34}_{-0.24}$	–
J1150+1501	< 100	1200 ± 920	8.14 ± 0.10	-1.52 ± 0.31	6.63 ± 0.17	$-0.03^{+0.29}_{-0.23}$	$2.14^{+0.28}_{-0.30}$	–
J1157+3220	< 100	–	8.46 ± 0.22	-1.42 ± 0.37	7.04 ± 0.21	$0.55^{+0.21}_{-0.42}$	$2.62^{+0.32}_{-0.18}$	3
J1200+1343	172 ± 53	–	8.16 ± 0.06	-1.04 ± 0.24	7.12 ± 0.14	$-0.18^{+0.20}_{-0.16}$	$1.19^{+0.47}_{-0.42}$	–
J1225+6109	< 100	–	8.02 ± 0.05	-1.65 ± 0.31	6.37 ± 0.15	$-0.08^{+0.26}_{-0.26}$	$2.12^{+0.34}_{-0.24}$	4
J1253−0312	437 ± 35	470 ± 320	8.02 ± 0.03	-0.92 ± 0.21	7.09 ± 0.12	$0.37^{+0.15}_{-0.15}$	$1.46^{+0.51}_{-0.23}$	–
J1314+3452	180 ± 15	–	8.27 ± 0.11	-1.52 ± 0.30	6.76 ± 0.18	$0.49^{+0.23}_{-0.55}$	$2.72^{+0.30}_{-0.21}$	2
J1323−0132	628 ± 100	214 ± 140	7.72 ± 0.01	-1.16 ± 0.18	6.55 ± 0.11	$-0.52^{+0.08}_{-0.09}$	$0.51^{+0.26}_{-0.10}$	–
J1359+5726	< 100	2070 ± 2240	7.99 ± 0.07	-1.38 ± 0.22	6.62 ± 0.14	$-0.32^{+0.20}_{-0.14}$	$1.67^{+0.31}_{-0.26}$	–
J1416+1223	295 ± 61	–	8.15 ± 0.04	-0.84 ± 0.06	7.31 ± 0.06	$0.10^{+0.21}_{-0.25}$	$2.12^{+0.32}_{-0.26}$	–
J1418+2102	< 100	1150 ± 150	7.51 ± 0.03	-1.46 ± 0.23	6.05 ± 0.15	$-0.52^{+0.15}_{-0.16}$	$0.83^{+0.49}_{-0.35}$	–
J1428+1653	119 ± 62	–	8.21 ± 0.14	-1.13 ± 0.25	7.08 ± 0.17	$-0.49^{+0.26}_{-0.19}$	$1.85^{+0.15}_{-0.23}$	–
J1429+0643	< 100	–	7.95 ± 0.06	-1.11 ± 0.19	6.84 ± 0.14	$-0.18^{+0.11}_{-0.17}$	$1.20^{+0.35}_{-0.21}$	–
J1444+4237	< 100	–	7.38 ± 0.09	-1.20 ± 0.30	6.19 ± 0.20	$-0.98^{+0.11}_{-0.08}$	$1.44^{+0.17}_{-0.17}$	–
J1448−0110	120 ± 29	–	8.07 ± 0.03	-1.36 ± 0.21	6.71 ± 0.14	$0.05^{+0.13}_{-0.14}$	$1.27^{+0.41}_{-0.24}$	2
J1521+0759	< 100	–	8.67 ± 0.07	-1.43 ± 0.16	7.24 ± 0.11	$-0.32^{+0.16}_{-0.17}$	$1.73^{+0.29}_{-0.30}$	–
J1525+0757	186 ± 60	–	8.76 ± 0.05	-1.22 ± 0.08	7.53 ± 0.08	$-0.35^{+0.69}_{-0.24}$	$2.75^{+0.28}_{-0.42}$	–
J1545+0858	153 ± 15	1750 ± 260	7.75 ± 0.02	-1.40 ± 0.18	6.35 ± 0.13	$-0.24^{+0.13}_{-0.17}$	$0.91^{+0.43}_{-0.26}$	–
J1612+0817	484 ± 88	–	8.47 ± 0.04	-0.96 ± 0.07	7.51 ± 0.07	$0.06^{+0.28}_{-0.24}$	$2.26^{+0.28}_{-0.26}$	–

Note. [References] (1) B. L. James et al. (2009), (2) WR candidates with FWHM $\gtrsim$ 500 km s^{-1} (see Section 4), (3) D. Miralles-Caballero et al. (2016), (4) A. Paswan, A. Omar & S. Jaiswal (2019). †The n_e[Ar IV] derived in this study are in agreement with the values reported in M. Mingozzi et al. (2022).

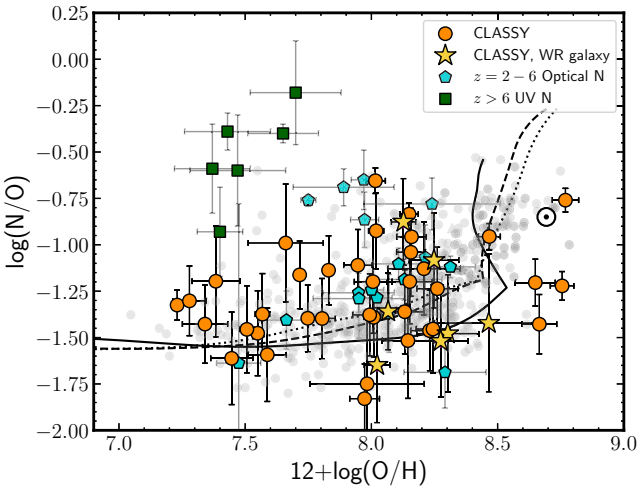

Figure 2. The N/O–O/H relation for the CLASSY sample. CLASSY galaxies hosting WR stars are also identified (star symbols), and they show similar N/O ratios to the bulk of the sample, with the exception of the WR galaxy Mrk 996 (B. L. James et al. 2009), which exhibits an N/O enhancement. The comparison sample of local SFGs and H II regions (small circles) was compiled and re-analysed in K. Z. Arellano-Córdova et al. (2024). A sample of high-redshift galaxies is included for comparison. SFGs at $z = 2$–6 with N/O ratios derived from optical [N II] lines are shown as pentagons (R. L. Sanders et al. 2023a; N. S. J. Rogers et al. 2024; K. Z. Arellano-Córdova et al. 2025; D. Scholte et al. 2025; B. Welch et al. 2025; Y. Zhang, T. Morishita & M. Stiavelli 2025), while the squares represent $z > 6$ galaxies with N/O derived from UV nitrogen lines (Y. Isobe et al. 2023; T. Jones et al. 2023; K. Nakajima et al. 2023; R. L. Sanders et al. 2023b; K. Z. Arellano-Córdova et al. 2024; R. Marques-Chaves et al. 2024; D. Schaerer et al. 2024; M. W. Topping et al. 2025a). The different curves show predictions from chemical evolution models with an infall mass of $\log(M_{\rm inf}) = 10$ $M_\odot$, SFEs of 0.5, 1, and 5 $\rm Gyr^{-1}$, and a time infall of $\tau_{\rm inf} = 0.1$ Gyr represented by solid, dashed, and dotted lines, respectively (F. Vincenzo et al. 2016). The CLASSY galaxies (circles) follow the expected N/O–O/H relation and occupy a similar parameter space as SFGs at $z = 2$–6. In contrast, they differ from the $z > 6$ population, showing no apparent redshift evolution.

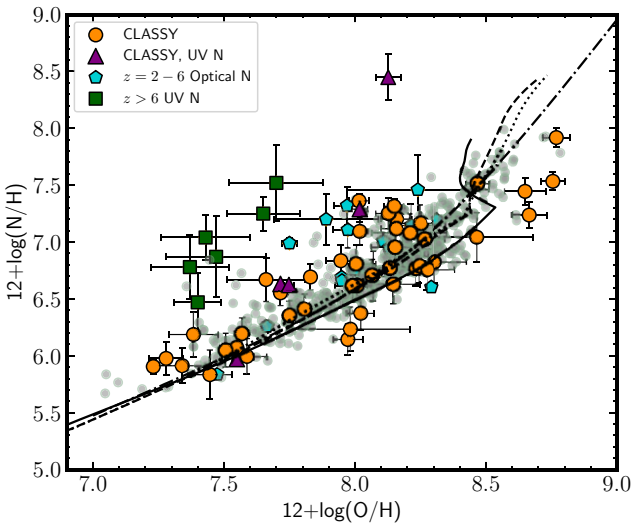

Figure 3. The N/H–O/H relation for CLASSY and the sample of high-redshift galaxies. SFGs at $z = 2$–6 from R. L. Sanders et al. (2023b), B. Welch et al. (2025), N. S. J. Rogers et al. (2024), K. Z. Arellano-Córdova et al. (2025), D. Scholte et al. (2025), and Y. Zhang et al. (2025) in pentagons, while the squares represent $z > 6$ galaxies from R. Marques-Chaves et al. (2024), M. W. Topping et al. (2024b), M. W. Topping et al. (2025a), M. Curti et al. (2025), and D. Schaerer et al. (2024). For comparison, we include the local sample in small circles. High-redshift galaxies are shifted to higher values of N/H, mainly those galaxies using UV nitrogen lines (squares), while the optical N sample at $z = 2$–6 follows the trend of CLASSY at $z \sim 0$. The purple triangles show those CLASSY galaxies with N/O derived using UV [N IV] or [N III] lines (see Z. Martinez et al. 2025). The different curves show the predictions of chemical evolution models for the N/H–O/H relation, as in Fig. 2, while the dash–dotted line represents an empirical calibration to SDSS galaxies from S. R. Flury & E. C. Moran (2020).

While at $z > 6$, the sample of SFGs shows a significantly high N/O for $12 + \log(\rm O/H) < 8$ as reported in their original studies. Moreover, the UV and optical N/O abundances occupy two different positions in the N/O–O/H relation. This could suggest that optical and UV lines trace different zones of the nebula (e.g. M. Pascale et al. 2023; M. W. Topping et al. 2024b). In Section 5, we will provide a detail comparison of CLASSY and high-z galaxies.

To inspect the chemical enrichment of the CLASSY galaxies in the N/O–O/H relation, we have included chemical evolutions models of F. Vincenzo et al. (2016) in Fig. 2 (see also N. Kumari et al. 2018; C. Hayden-Pawson et al. 2022). We have selected three different models covering the following parameters: an infall mass of $\log(\rm M_{infall}/M_\odot) = 10$, SFE of $\nu = 0.5$ $\rm Gy^{-1}$ (dotted), $\nu = 1$ $\rm Gy^{-1}$ (dashed), and $\nu = 5$ $\rm Gy^{-1}$ (solid), time fall $\tau = 1$ Gyr and a mass loading factor $\omega = 1.0$. These models assume a E. E. Salpeter (1955) IMF. Overall, most CLASSY galaxies follow the evolutionary track by the chemical evolution models, but the observations show high scatter. However, most galaxies exhibit higher N/O ratios at a fixed metallicity. In principle, a higher SFE should result in an increase in N/O due to the early contribution of intermediate massive stars (F. Vincenzo et al. 2016). We stress that, since galaxies have different star formation histories, it is necessary to compare the observed N/O–O/H relation with models different star formation history and feedback in order to properly interpret the observed relation in Fig. 2 (see e.g. C. Kobayashi & A. Ferrara 2024; S. Bhattacharya & C. Kobayashi 2025).

4.2 The N/H versus O/H relation

We also explore the relation between the total N/H and O/H for CLASSY shown in Fig. 3. Additionally, we have added the sample of local SFGs and H II regions from the literature. As expected, we find a correlation between these two abundance ratios due to nucleosynthesis of intermediate and massive stars. For comparison, we have added the same chemical evolution models as in Fig. 2, together with the empirical N/H–O/H relation for SDSS SFGs from S. R. Flury & E. C. Moran (2020), which is consistent with the observed trends.

Then, we have also incorporated the high-redshift for comparison in Fig. 3. First, we found that galaxies with optical N abundance determination follow the same abundance pattern as CLASSY for a metallicity range of $12 + \log(\rm O/H) = 7.5$-8.5. In contrast, galaxies at $z > 6$ showing $12 + \log(\rm O/H) < 8.0$ are shifted to higher values of $12 + \log(\rm N/H)$. This might be due to the high N/O and very low metallicity of $z > 6$ galaxies (squares) derived from their physical conditions (M. J. Hayes et al. 2025; Z. Martinez et al. 2025). As an inspection, we have added the N/H values for five galaxies with UV N emission lines (J0127−0639, J1253−0132, J1044+0353, and J1545+058) reported in Z. Martinez et al. (2025). Fig. 3 shows that CLASSY galaxies with N/H derived using both UV (purple triangles) and optical N lines exhibit a similar abundance patterns within the uncertainties. Overall, the differences between UV and optical N/O

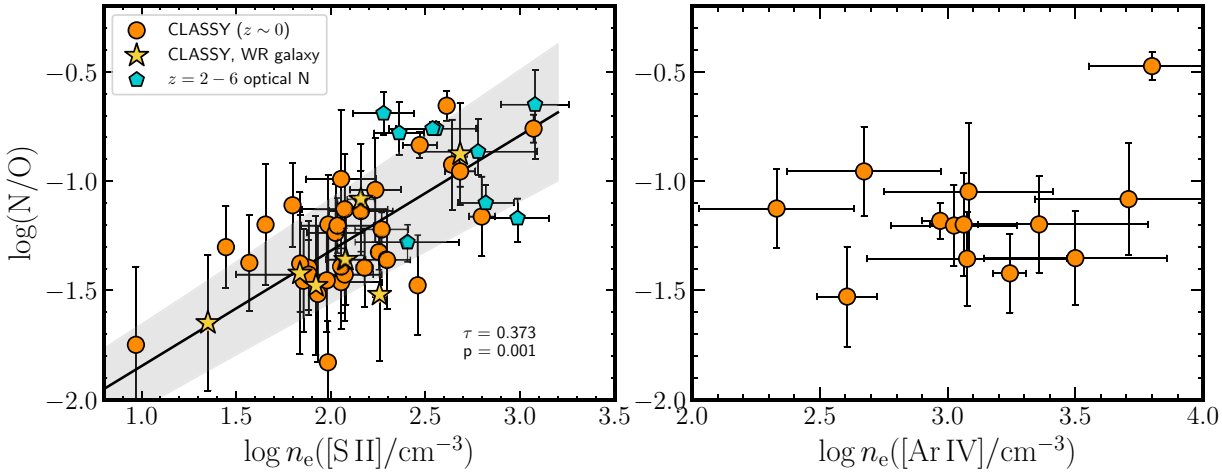

Figure 4. *Left*: N/O abundances as a function of low-ionization density, n_e[S II]. SFGs at $z > 2$ are also included for comparison from R. L. Sanders et al. (2023a), K. Z. Arellano-Córdova et al. (2025), D. Scholte et al. (2025), T. M. Stanton et al. (2025), and B. Welch et al. (2025). We find that high density derived from n_e[S II] correlates with the high values of N/O for local galaxies (with a Kendall's coefficient of $\tau = 0.372$ and p-value $= 0.001$), while $z = 2$–6 galaxies show a similar trend. The stars are galaxies with WR stars features. The best fit to the data for the N/O versus log(n_e[S II]) is shown in solid line for CLASSY. *Right*: the N/O ratios as a function of high-ionization density, n_e[Ar IV]. N^+ and O^+ were derived using n_e[Ar IV] for 13 CLASSY galaxies. Only three CLASSY galaxies have measurements of both n_e[S II] and n_e[Ar IV] within a similar range of n_e = 200–600 cm^{-3}. J0808+3948 shows the highest values, with n_e = 1200–6310 cm^{-3} and log(N/O) $= -0.47$ to -0.65 when derived using both density diagnostics.

abundances for CLASSY can reach 0.08−0.28 dex in N/H, with the exception of J0127−0639, which exhibits a difference of 1.2 dex. J0127−0639 (or Mrk996) is an object with complex kinematics and chemical enrichment. As seen in Fig. 3, Mrk 996 exhibits a very high N/H ratio that departs significantly from the bulk of the sample. This difference is likely due to the presence of WR stars in combination with their exotic kinematics, which can enrich N/O regardless of whether optical or UV nitrogen lines are used (B. L. James et al. 2009) (see also Fig. 2). A detailed discussion of UV N/O galaxies (including Mrk 996) is presented in Z. Martinez et al. (2025). In the following sections, we will analyse the physical conditions and properties of the CLASSY galaxies to better understand the high scatter in the N/O–O/H relation.

4.3 Electron density

The electron density, usually calculated using the [S II] λλ6717,31 lines, and T_e are crucial physical conditions to determine the chemical composition of the gas. For objects with $n_e \leq 100$ cm^{-3}, the inferred abundances are less sensitive to density (e.g. D. E. Osterbrock 1989; M. Peimbert, A. Peimbert & G. Delgado-Inglada 2017). For high density objects $n_e \geq 300$ cm^{-3}, the N/O is less explored since if density diagnostics are not available or are very uncertain might introduce bias in the determination of N/O (e.g. G. Stasinska 2023; Y. Zhang et al. 2025). M. Mingozzi et al. (2022) presented an analysis of the density structure of CLASSY galaxies by comparing density estimates that correspond to low-, intermediate-, and high-ionization regions (such as n_e[S II], n_e[Cl III], and n_e[Ar IV], respectively). These authors found no significant impact on metallicity using different density diagnostics on the metallicity inferred for the CLASSY galaxies, while N/O was not explored in that study.

In the left panel of Fig. 4, we compare the N/O ratio as a function of n_e[S II]. We have used the Kendall's τ coefficient to verify any potential correlation between N/O and n_e[S II]. We find a correlation between N/O and n_e[S II] (with a p-value $= 0.001$, $\tau = 0.373$), showing that high density objects, log(n_e[S II]/cm^{-3}) ≥ 2.5 are shifted to high N/O ratios.

Our best fit using orthogonal distance regression (ODR, P. T. Boggs et al. 1981; P. Virtanen, R. Gommers & T. E. Oliphant 2020) to the relation between N/O and n_e is as follow:

$$\log(\mathrm{N/O}) = (0.432 \pm 0.071) \times \log(\mathrm{n_e}) - (2.166 \pm 0.0150). \quad (1)$$

To analyse the result presented in the left of Fig. 4, we have also determined the N/O ratios using n_e[Ar IV], which traces the high ionization density structure of the gas. For 13 CLASSY galaxies we recalculated the N/O ratios adopting n_e[Ar IV] instead of n_e[S II] (see the right panel of Fig. 4). For such galaxies, we measure 2.5 $<$ log(n_e[Ar IV]/cm^{-3}) $<$ 3.2, while the same galaxies also show 2 $<$ log(n_e[S II]/cm^{-3}) $<$ 3. Note that the density range derived for these galaxies depends on the sensitivity of the diagnostic used (e.g. J. E. Méndez-Delgado et al. 2023b). We find that the differences in N/O using different density measurements can reach values of up to 0.2−0.3 dex higher, with some exception showing values up to 0.1 dex lower. It implies that N/O might be affected by the density structure of the gas, which is particularly associated with the [O II] λλ3726,29 to calculate O^+ (see J. E. Méndez-Delgado et al. 2023a; G. Stasinska 2023), due to the low critical density of those lines (L. Juan de Dios & M. Rodríguez 2017). In contrast to the correlation between N/O and n_e[S II], there is no correlation between N/O and n_e[Ar IV] (see the right panel of Fig. 4). Of the seven CLASSY galaxies with high N/O and n_e[S II], only three have n_e[Ar IV] measurements (see Table 2). While two of them show good agreement between the values of n_e[S II] and n_e[Ar IV], J0808+3948, with high density in both diagnostics, shows an increase in log(N/O), with a value 0.28 dex higher when n_e[Ar IV] is used. A larger sample of galaxies with both n_e[S II] and n_e[Ar IV] is needed to better understand the role of n_e in the high N/O ratios of galaxies at $n_e >$ 300 cm^{-3} (e.g. J. E. Méndez-Delgado et al. 2023b; H. Yanagisawa et al. 2024b; Z. Martinez et al. 2025).

On the other hand, in Z. Peng et al. (2025), the authors determined the gas density for 14 CLASSY galaxies, reporting measurements of [O II] λλ3726,29 and [S II] λλ6717,31 for different gas components derived from the high-resolution spectra. Interestingly, n_e[S II]λλ6717,31 derived from the narrow component is

relatively higher than the values analysed in this study (e.g. K. Z. Arellano-Córdova et al. 2022a, see also AC24a). For example, for J0808+3948, the object with the highest n_e[S II] λλ6717,31 in the CLASSY sample, we derived a value of n_e[S II] ∼ 1200 cm^{-3}, while the value reported in Z. Peng et al. (2025) is a factor of 3.5 higher. In contrast, their values for n_e[O II] are aligned with our measurements. We give a look at the values reported for n_e[S II] for the 14 CLASSY galaxies reported in Z. Peng et al. (2025) from the narrow component, and we find significant differences of up to 650 cm^{-3} higher for most of the galaxies than our measurements. We think that aperture effects should be minimal since in K. Z. Arellano-Córdova et al. (2022a), these authors show a good agreement between n_e[S II] derived in galaxies with different aperture sizes and instruments when the relative fluxes are used to derive the physical conditions and metallicities. A follow-up of the density structure of CLASSY will provide information on its impact on the chemical abundance ratios in the high density regime. Since Z. Peng et al. (2025) did not report the N/O ratios in their study, we have derived N/O using the extinction-corrected fluxes of the narrow component and the physical conditions of their study. In this inspection to the N/O ratios, we find consistent results with our result in Fig. 4, implying that N/O increases as n_e increases for most of the galaxies of the sample. In Fig. 4, we have also identified those CLASSY galaxies with WR star features, which are located in the low-density regime (log(n_e[S II]/cm^{-3}) ∼2, with exception of Mrk 996). Moreover, for comparison, we added the high-z sample with optical N/O ratios. We find that high density galaxies at $z = 2 - 6$ with high N/O aligns with our finding at $z \sim 0$.

Therefore, from Fig. 4, we suggest that part of the dispersion in the N/O–O/H relation can be associated with the density structure of the nebula, implying that intrinsically high density objects ($n_e \gtrsim$ 300 cm^{-3}) might result in high N/O abundances. However, a large sample of galaxies covering high density structure by different diagnostics is necessary to confirm the results present in Fig. 4. In Section 5, we discuss these results in comparison with other studies.

4.4 Global galaxy properties

The scatter of the N/O–O/H relation could be related to different processes such as the star formation history of the galaxies, the time delay of the primary and secondary contribution of N, the enrichment by WR stars, accretion of metal-poor gas, the temperature and density structure used to determine N/O, the impact of the SFE in regulating the yield production of O and N, among others (e.g. R. B. C. Henry et al. 2000; J. Köppen & G. Hensler 2005; A. Nava et al. 2006; R. O. Amorín et al. 2010; R. Amorín et al. 2012; E. Pérez-Montero et al. 2013; F. Vincenzo et al. 2016; K. Z. Arellano-Córdova & M. Rodríguez 2020; D. A. Berg et al. 2020; C. Hayden-Pawson et al. 2022) We investigate the impact of various galaxy properties such as stellar mass, SFR and SFR surface density on the N/O and N/H ratios for CLASSY and its evolution across redshifts. These physical measurements were derived from previous CLASSY papers (see Section 2). In our analysis, we include the sample local SFGs and high-z galaxies described in Section 2.3.

Fig. 5 shows the comparison of the N/O and N/H ratios as functions of stellar mass (left), SFR (middle) and specific SFR (sSFR, right). We discuss our findings for the CLASSY sample and their comparison with the properties of galaxies at high-z in Section 5. Note that in Fig. 5, we have also distinguished galaxies whose N/O is derived either using UV or optical emission lines of N for comparison purposes.

4.4.1 *Stellar mass*

Stellar mass is strongly linked with the chemical evolution of galaxies. Previous studies have found a positive correlation between N/O and M$_\star$ in galaxies, implying that more massive galaxies are chemically enriched from different generations of stars.(e.g. E. Pérez-Montero & T. Contini 2009; R. O. Amorín et al. 2010; C. Hayden-Pawson et al. 2022; A. L. Strom et al. 2022).

The left panels of Fig. 5 show the relation between stellar mass and N/O (top) and N/H (bottom) for CLASSY. We find a significant positive correlation (Kendall's coefficient of τ =0.293 and p-value = 0.005) between N/O and the stellar mass with some scatter across masses. We also note that the sample of dwarf galaxies (z ∼0) compiled from the literature are also in agreement with the distribution of CLASSY (small circles, see also Section 2.3).

We have used the expression reported in C. Hayden-Pawson et al. (2022, see their equation 4) to provide a relation between stellar mass and the N/O ratios calculated using the T_e-sensitive method. The reason for the selection of this relation is due to the shape of the N/O-M⋆ relation as stellar mass increases, log(M⋆/M$_\odot$) > 10 (e.g. E. Pérez-Montero & T. Contini 2009; E. Pérez-Montero et al. 2013; R. L. Sanders et al. 2021). The parameter of the fit are as follows: log(N/O)$_0$ $= -1.37 \pm 0.05$, log(N/O)$_1$ $= -0.98 \pm 0.11$, log(M$_0$/M$_\odot$) $= 9.10 \pm 0.18$, and $k = 3$, where k is the transition between low (N/O$_0$) and high plateaus (N/O$_1$) and M$_0$ indicates where the shape of the relation start to decrease (C. Hayden-Pawson et al. 2022, see their equation 4). From our best fit in Fig. 5, we have found a well-defined plateau of N/O below log(M⋆/M$_\odot$) ∼ 9. At log(M⋆/M$_\odot$) > 9 the fit rapid increases with N/O.

In Fig. 5, we have added the N/O versus stellar mass relation derived by B. H. Andrews & P. Martini (2013) for stacked SDSS galaxies at $z \sim 0$ (solid line), where N/O and O/H were obtained using the T_e-sensitive method. This relation exhibits a break, with two distinct components across different metallicity regimes. At low metallicity (log(M⋆/M$_\odot$) < 8.5), N/O remains roughly constant with stellar mass, consistent with the behaviour seen in the CLASSY sample. In contrast, at higher metallicities, a positive correlation between N/O and M⋆ is observed. The slope of the high-metallicity N/O-M⋆ relation slightly overlaps with the CLASSY sample, which shows an offset towards lower stellar masses and higher N/O. We also compare our results with the relation presented in C. Hayden-Pawson et al. (2022) (dashed line in Fig. 5), which is based on a sample of local SFGs than span range of stellar masses (10^8-10^{11} $M_\odot$) and metallicities derived using strong-line methods. We noticed that for 8 < log(M$_\star$/M$_\odot$) < 9 this relation slightly aligns with the results of CLASSY. For higher stellar masses, CLASSY shows an elevated N/O ratio with some scatter (see also Section 5 for a discussion).

Additionally, we add the sample at $z = 2 - 6$ in Fig. 5 as a comparison. The $z = 2 - 6$ galaxies are shifted to higher N/O values compared to the relationship for the local SDSS sample by C. Hayden-Pawson et al. (2022). In Fig. 5, we also include the fit derived on the N/O-M⋆ relation at $z = 2 - 3$ galaxies by A. L. Strom et al. (2017, dash–dotted line). The N/O and O/H values were derived using a custom strong-line calibrator, showing a scatter of 0.17 dex around the N/O-M⋆ relation. The stellar masses for this relation range from 10^9 M$_\odot$ to 10^{11} M$_\odot$. A. L. Strom et al. (2017) found a moderate correlation with the stellar mass. However, there is a considerable scatter in the data of 0.33 dex, mainly attributed to the different time-scales for N being ejected into the ISM. In this comparison, we find that CLASSY galaxies are shifted to higher N/O values than the relation for $z = 2 - 3$ galaxies, indicating a

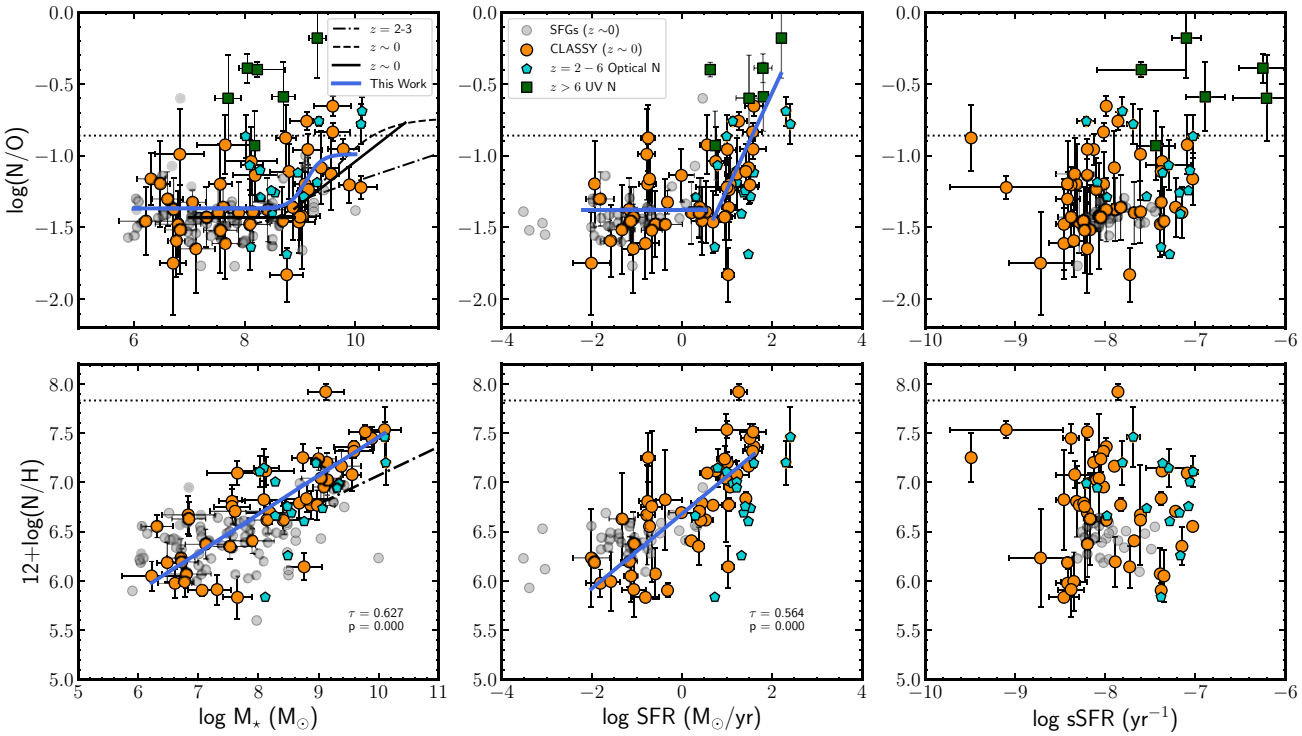

Figure 5. Comparison of the N/O and N/H ratios as a function of the stellar mass (left), SFR (middle), and sSFR (right) for CLASSY. The small circles indicate the sample of SFGs from D. A. Berg et al. (2012), D. A. Berg et al. (2016), D. A. Berg et al. (2019), and Y. I. Izotov et al. (2017). The dashed line shows the N/O versus M⋆ for SDSS galaxies derived by C. Hayden-Pawson et al. (2022), while the dash–dotted line represents the N/O versus M⋆ and N/H versus M⋆ relations from A. L. Strom et al. (2022) for galaxies at $z \sim 2$–3. Such relations were derived using strong-line methods. The dotted lines represent the solar value of N/O and N/H from M. Asplund et al. (2021). The pentagons represent galaxies at $z = 2$–6 and their N/O abundances on optical lines by R. L. Sanders et al. (2023a), B. Welch et al. (2025), K. Z. Arellano-Córdova et al. (2025), D. Scholte et al. (2025), and Y. Zhang et al. (2025), while that the squares represent galaxies at $z > 6$ based their N/O abundances on UV lines by Y. Isobe et al. (2023), R. Marques-Chaves et al. (2024), M. W. Topping et al. (2024b), M. W. Topping et al. (2025a), M. Curti et al. (2025), and D. Schaerer et al. (2024). Our best fit to the CLASSY data is shown in a solid blue line.

steeper relation between N/O and stellar mass. We also note that the sample of $z = 2 - 6$ galaxies (pentagons) shows N/O values that are offset from the relation found by A. L. Strom et al. (2017) at similar redshifts.

For N/H against M⋆, we found a positive strong correlation (τ =0.627, p-value $< 10^{-3}$) as stellar mass increases, probably because the dependency between N/H and O/H (see Fig. 3), which is implicit in the determination of N/H $=$ N/O $\times$ O/H. Our best fit to the data show slope and intercept of 0.391 ± 0.043 and 3.55 ± 0.356 (see the bottom panel of Fig. 5). In the same panel, we also show the relation between N/H and stellar mass from A. L. Strom et al. (2017), which is flatter than the one calculated in this work for the same range of stellar masses. We also note that the galaxies at high-z are located in the same parameter space than the CLASSY sample at $z \sim 0$. A. L. Strom et al. (2017) also provided the N/H-M⋆ relation which is displayed in the bottom panel of Fig. 5. We find that for $\log(M_\star/M_\odot) > 9$, CLASSY and the high-$z$ sample show a steeper relation with less scatter in comparison to the relation at $z = 2 - 3$ by A. L. Strom et al. (2017).

In summary, we have confirmed that N/O increases with the stellar mass with some of scatter at $\log(M_\star/M_\odot) > 8$ which might be associated with the secondary production of N by intermediate massive stars (see also E. Pérez-Montero et al. 2013) (see also 5). From our comparison with the high-z sample, there is no apparent redshift evolution up to $z \sim 6$.

4.4.2 SFR and sSFR

The relation between N/O and SFR in concert with $M_\star$ has previously been studied by E. Pérez-Montero & T. Contini (2009), E. Pérez-Montero et al. (2013), and C. Hayden-Pawson et al. (2022). E. Pérez-Montero et al. (2013) reported any secondary dependence of the N/O-$M_\star$ with SFR, which makes N/O insensitive to the inflows of metal-poor gas, while that the opposite was found by C. Hayden-Pawson et al. (2022) in local galaxies. Such a discrepancy is mainly associated for the different strong-line method selected in each study.

Following our analysis with CLASSY with T_e-sensitive chemical abundances, we report the N/O−SFR relation in the top/middle panel of Fig. 5. The N/O−SFR relation shows a well-defined plateau below $\log(SFR/M_\odot\ yr^{-1}) < 1$, while there is also a positive correlation with N/O as SFR increases. We have also fitted the N/O−SFR relation using to different slopes indicated in solid blue line on Fig. 5. Our best fits to the data corroborate the plateau at lower SFR with a mean of $\log(N/O) = -1.38 \pm 0.20$. As the SFR increases, the slope of the fit changes abruptly at $\log(SFR/M_\odot\ yr^{-1}) \sim 1$. For the N/O−SFR plane, we derive $\log(N/O) = (0.67 \pm 0.20) \times \log(SFR/M_\odot\ yr^{-1}) - (1.91 \pm 0.23)$. For the correlation between high N/O and high SFR, we derive a Kendall's coefficient of $\tau = 0.538$ and p-value$= 0.010$, indicating that ongoing star formation activity probably contributes to the nitrogen production by intermediate massive stars in more evolve systems. We also investigated the relation between N/H and SFR, as shown in the bottom/middle panel of Fig. 5. For N/H, there is

a positive correlation, as in the case of N/O, as SFR increases. Our fit shows a smooth increase of N/H with SFR, unlike the abrupt increase observed between N/O and SFR, possibly due to the dependence of O/H on the total abundance of N/H. For the N/H-SFR relation, we derived a slope and intercept as follow: $\log(\mathrm{N/H}) = (0.378 \pm 0.050) \times \log(\mathrm{SFR/M_{\odot}\ yr^{-1}}) + (6.68 \pm 0.05)$, with a Kedall's tau coefficient and p-value of $\tau = 0.564$ and p-value $< 10^{-3}$, respectively.

Finally, the right column of Fig. 5 shows the relationship between N/O and N/H as a function of sSFR. Overall, there is no clear correlation between N/O and sSFR, since the variations in N/O can reach up to 0.5 dex for a fixed sSFR. Similarly, the comparison between N/H and sSFR shows results akin to those for N/O (see the bottom/right panel of Fig. 5), with no correlation between these two quantities. The fact that SFR and mass together produce no correlation may instead indicate that the long-term and short-term chemical enrichment pathways contribute equally to the N/O abundance pattern. While no correlation exists between N/O and sSFR, significant scatter persists in sSFR at a given N/O for which statistical uncertainty cannot account. This dispersion may indicate physical variations in the mass assembly history (N production, stellar mass) and instantaneous enrichment (O production, SFR) which contribute to the observed abundance patterns.

4.4.3 $\Sigma_{M_\star}$ and Σ_{SFR}

Previous studies have indicated that the N/O enhancement in galaxies at high-z is related to its compactness (e.g. N. A. Reddy et al. 2023a, b; R. Marques-Chaves et al. 2024; D. Schaerer et al. 2024; M. W. Topping et al. 2025), which correlates with high star formation surface density (Σ_{SFR}) and stellar mass density ($\Sigma_{M_\star}$). In this context, we have derived $\Sigma_{\rm SFR}$ and $\Sigma_{M_\star}$ for CLASSY to compare with the N/O and N/H abundance ratios at $z \sim 0$. These physical properties can provide information of the intensity of SFR encapsulated by the half-light radii ($r_{\rm eff}$) in their impact on the observed abundance patterns of N. For CLASSY, we have taken measurements for $r_{\rm eff}$ from D. A. Berg et al. (2022) (see also Section 2.2). Such as sizes range from 0.78″to 7.99″ (0.11 − 2.85 kpc). Then, we determine stellar mass and SFR surface density as $\Sigma_{SFR} = \mathrm{SFR}/(2\pi\, r_{\rm eff}^2)$ and $\Sigma_{M_\star} = M_\star/(2\pi\, r_{\rm eff}^2)$. To compare our results with galaxies at $z > 2$, we have also compiled $\Sigma_{\rm SFR}$ and $\Sigma_{M_\star}$ from the original studies. When these measurements are not available, we calculate $\Sigma_{\rm SFR}$ and $\Sigma_{M_\star}$ using their report values of SFR and $r_{\rm eff}$ (i.e. R. Marques-Chaves et al. 2024; D. Schaerer et al. 2024; M. W. Topping et al. 2024b, a; M. Curti et al. 2025; Y. Zhang et al. 2025).

The top panels of Fig. 6 shows the comparison of N/O and N/H ratios against $\Sigma_{\rm SFR}$ for CLASSY. We find a moderate positive correlation between N/O and the SFR surface density with Kendall's $\tau = 0.226$ and a p-value of 0.030. It implies that galaxies with higher star formation activity exhibit elevated N/O ratios (see also Fig. 5), although with some scatter around the fit of $\sigma = 0.25$ dex. We have determined a slope and intercept of $a = 0.29 \pm 0.09$ and $b = -1.19 \pm 0.05$, respectively, considering the uncertainties in both axis. For N/H, we report a significant correlation between the $12 + \log(\mathrm{N/H})$ and $\Sigma_{\rm SFR}$, with Kendall's coefficient of $\tau = 0.408$ and p-value of p-value $< 10^3$. The best fit to the data implies a slope of $a = 2.20 \pm 0.42$ and an intercept of $b = 7.25 \pm 0.16$, respectively, with a scatter around the fit of $\sigma = 0.32$ dex.

On the other hand, the bottom panel of Fig. 6 shows a poor correlation between the N/O versus $\Sigma_{M_\star}$, which is indicated for a Kendall's coefficient of $\tau = 0.091$. In contrast, we find a significant correlation between $12 + \log(\mathrm{N/H})$ and the stellar mass surface density, probably because of the metallicity is involved in the calculations of N/H (see also Fig. 5). Our best fit for such relation provides a slope and intercept of $a = 1.20 \pm 0.19$ and $b = 4.63 \pm 0.351$, respectively.

4.5 Feedback and N/O enrichment

Galactic outflows play an essential role in regulating galaxy evolution (e.g. T. M. Heckman et al. 2011, 2015). Optical emission lines such as Hβ and [O III] λ5007 have been widely used to trace signatures of outflowing gas associated with winds from massive stars or AGN activity (e.g. D. K. Erb 2015; J. Chisholm et al. 2017; L. Hogarth et al. 2020; M. Mingozzi et al. 2022; S. R. Flury, E. C. Moran & M. Eleazer 2023; R. O. Amorín et al. 2024; L. Komarova et al. 2025; Z. Peng et al. 2025). While optical lines provide valuable information on the kinematics of ionized gas, UV low-ionization absorption lines trace the neutral outflowing gas, offering complementary insights into the multiphase nature of outflows and the processes that drive them (e.g. T. M. Heckman et al. 2015; B. L. James et al. 2015; S. Hernandez et al. 2020; X. Xu et al. 2022; S. R. Flury et al. 2023; M. J. Hayes & C. Scarlata 2023; K. S. Parker et al. 2024; X. Xu et al. 2025).

To understand the impact of outflows driven by stellar winds on the N/O ratio, we use the offset velocity ($v_{\rm out}$) and mass outflow rate ($\dot{M}_{\rm out}$) measurements reported by X. Xu et al. (2022) for CLASSY using UV absorption lines. In the bottom panel of Fig. 7, we show a moderate correlation between outflow velocity and the N/O ratio, colour-coded by $v_{\rm out}$ (Kendall's $\tau = -0.472$, p-value $= 0.002$). This correlation implies that CLASSY galaxies with high-velocity outflows tend to exhibit elevated N/O ratios (see also James et al., submitted, for a multiphase gas analysis of N). We also note that galaxies with high-velocity outflows generally have relatively high metallicities and high $n_{\rm e}$. These findings suggest that the scatter in the N/O–O/H relation at $12 + \log(\mathrm{O/H}) \gtrsim 8$ reflects an interplay between SFR, electron density, and feedback-driven enrichment. Indeed, empirical scaling relations between stellar mass, SFR, metallicity, outflow velocity, and gas content together imply this feedback-driven interplay among these properties (e.g. J. Chisholm et al. 2018; S. R. Flury et al. 2023).

Additionally, we calculate the mass-loading factor ($\eta = \dot{M}_{\rm out}/\mathrm{SFR}$), which indicates the efficiency of feedback (or the relative strength of the outflow) from young (1–10 Myr) stellar populations normalized to the number of massive stars. There are important implicit dependencies in the estimation of $\dot{M}_{\rm out}$ that should be kept in mind in our analysis of feedback and chemical enrichment, such as $v_{\rm out}$ and the outflow radius (see equation 13 in X. Xu et al. 2022). X. Xu et al. (2022) reported a strong anticorrelation between the mass-loading factor and both $v_{\rm out}$ and M★, implying that strong outflows also seem to be more prevalent in low-mass galaxies and which we interpret as evidence for gravitational suppression of feedback. The comparison between N/O and η is shown in the bottom panel of Fig. 7, colour-coded by M★. We find a strong correlation between N/O and η (Kendall's $\tau = 0.317$, p-value $> 10^{-3}$), suggesting that feedback from stellar winds becomes relatively weak as N/O increases. Our fit to the data is as follows:

$$\log(\mathrm{N/O}) = (-0.266 \pm 0.045) \times \eta - (1.198 \pm 0.038). \quad (2)$$

This correlation could indicate that, at high stellar mass, metals are more likely retained and mixed with the surrounding ISM rather than expelled or recycled (e.g. A. Roy et al. 2021). Even as the feedback efficiency decreases, the velocity of the wind/outflowing gas does increase, which may further facilitate ready mixing. Overall, low-mass systems are more efficient in launching outflows, likely due to a

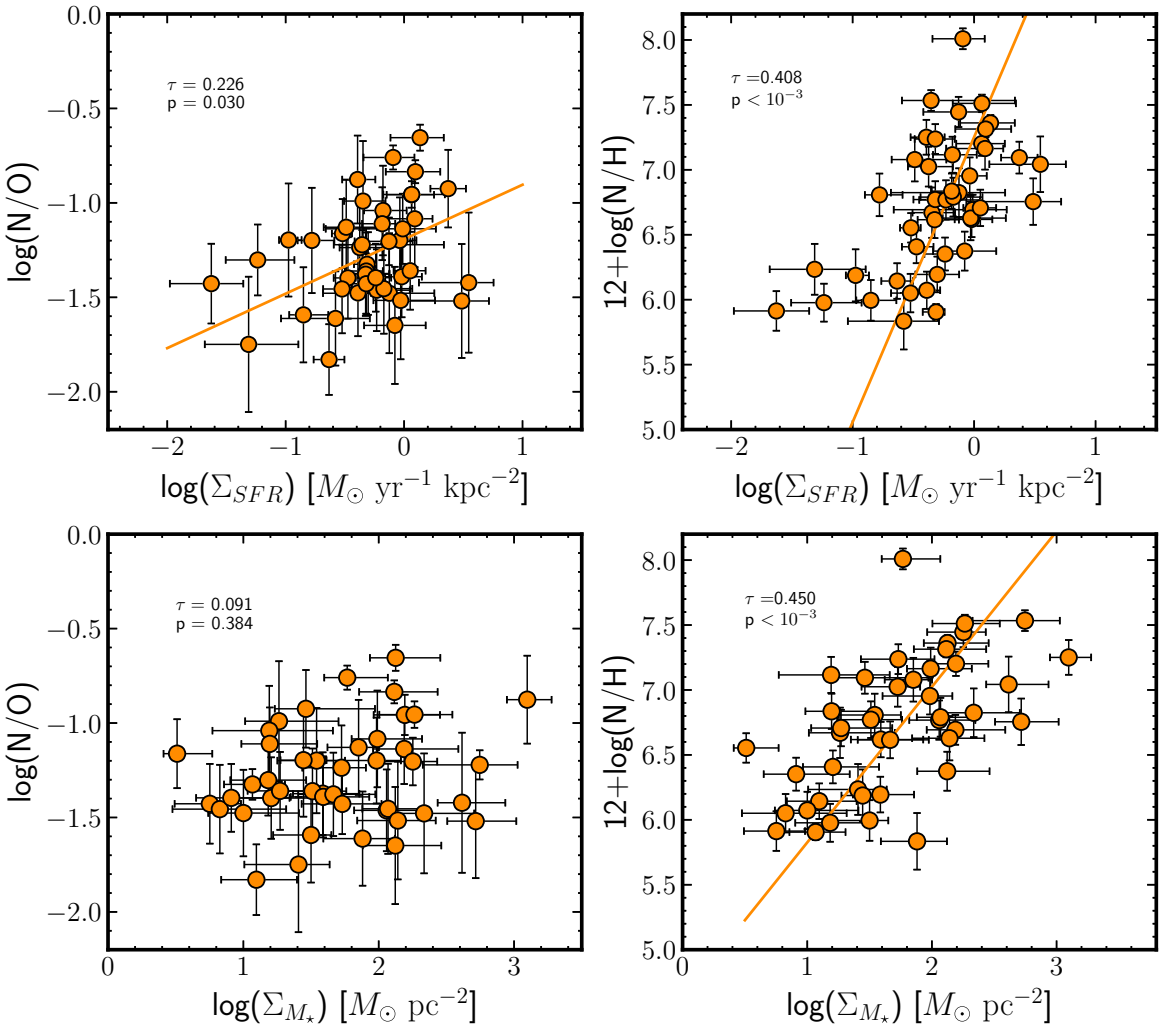

Figure 6. *Top:* the star formation surface density as a function of the N/O and N/H abundance ratios for CLASSY. *Bottom:* stellar mass surface density as a function of the N/O and N/H abundance ratios for CLASSY. The solid line represents the best fit to the data for CLASSY. The correlation between Σ_{SFR} and N/O indicates that compact objects show high values of N/O. The Kendall's coefficient of τ and the p-value are indicated in each panel.

combination of compactness (by connecting the mass–radius relation and mass–metallicity relation, e.g. T. I. Larsen, J. Sommer-Larsen & B. E. J. Pagel 2001), which increases the impact of feedback, and of reduced mass, which reduces gravitational suppression of feedback (e.g. A. L. Muratov et al. 2015; K. B. W. McQuinn, L. van Zee & E. D. Skillman 2019; M. Llerena et al. 2023). However, at fixed mass and radius, feedback tends to be more efficient at high metallicity as line driving is a dominant mechanism in stellar winds (e.g. C. Leitherer et al. 2014; C. M. Byrne et al. 2022). See Section 5 for more discussion.

5 DISCUSSION

We have analysed the gas properties and N/O and N/H abundances for the CLASSY survey high−z analogues based on T_e abundance determinations, and compared these results with high-z galaxies. Overall, we find that the CLASSY galaxies follow the trend of the N/O–O/H relation observed in other galaxies and H II regions at $z \sim 0$ with a significant scatter (see Fig. 2). In addition, we identify seven galaxies hosting WR stars, whose log(N/O) values (< -1.00) are consistent with those of other galaxies at similar metallicities with no N/O enhancement, except for J0127-0619 (Mrk 996 B. L. James et al. 2009). The large scatter in the N/O–O/H relation is well known and can be understood in terms of the different time-scales over which nitrogen and oxygen are released into the ISM (e.g. E. Pérez-Montero & T. Contini 2009; D. A. Berg et al. 2019) and different star formation histories (e.g. Y. Guo et al. 2016). Other galaxy properties may also play a crucial role in explaining part of this scatter. For example, F. Vincenzo et al. (2016), using chemical evolution models, show that the SFE significantly influences oxygen production by massive stars. If the SFE is low, small amounts of oxygen will be ejected to the ISM, implying an increase of the N/O abundance due to the production of N from different generations of stars (D. A. Berg et al. 2019; A. L. Schaefer et al. 2020). However, as shown in Fig. 2, variations in SFE ($\nu = 0.5$–5 Gyr^{-1}) do not fully explain the N/O scatter observed in the CLASSY galaxies with the selected chemical evolution models of (e.g. F. Vincenzo et al. 2016). We have analysed different galaxy properties that can have an important impact on the scatter around the N/O–O/H relation. In Appendices A and B, we provide additional analysis and discussion on the comparison between N/O and extinction, stellar ages, as well as comments on specific CLASSY galaxies related to gas kinematics

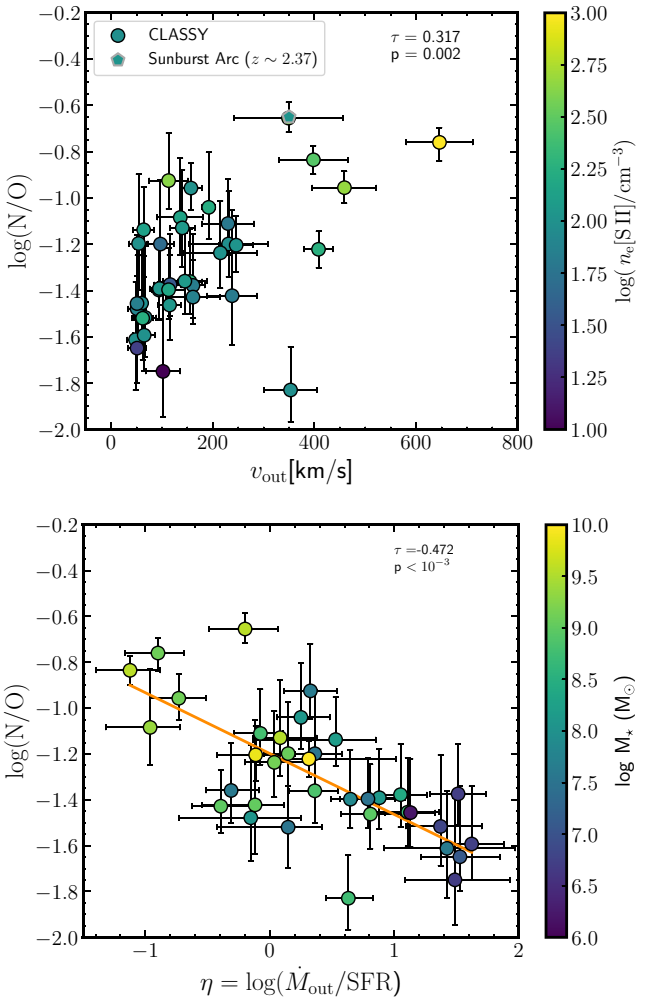

Figure 7. *Top:* N/O as a function of outflow velocity (v_{out}) (X. Xu et al. 2022), colour-coded by n_e for CLASSY. The Sunburst Arc galaxy is included for comparison with galaxies at $z \sim 0$. The outflow velocity and n_e values for Sunburst Arc are from R. Mainali et al. (2022) derived from both high ionization absorption and emission lines), while N/O is from B. Welch et al. (2025). *Bottom:* N/O as a function of mass-loading factor (η), colour-coded by stellar mass. The Kendall's τ coefficient and p-value are labelled in each plot. The solid line shows the best fit to the data. At high N/O, stellar feedback is stronger but less efficiently produced by young stellar populations.

and electron density. In the following sections, we analyse our main results from the previous sections.

5.1 The impact of electron density on N/O

In principle, the N^+/O^+ ratio is not sensitive to variations in T_e and n_e due to similar ionization potentials of these ions and their dependence on the critical densities in the low n_e regime (L. Juan de Dios & M. Rodríguez 2017). The variations of density ionized regions has been investigated by J. E. Méndez-Delgado et al. (2023a) in a large sample of galaxies and H II regions. These authors found that, in the presence of density fluctuations or multiple clumps of dense gas, the O^+ abundance is underestimated because n_e[S II] or n_e[O II] is insensitive to such high density clumps due to the desity regime that those diagnostics are valid (J. E. Méndez-Delgado et al. 2023b).

Similarly, our results indicate that high density gas traced by [S II] is associated with elevated N/O values (see Fig. 4). One possible explanation for this positive correlation between N/O and n_e is an underestimate of the ionic O^+ abundance derived from the [O II]λλ3726,29 lines in high density gas (e.g. J. E. Méndez-Delgado et al. 2023a; G. Stasinska 2023; Y. Zhang et al. 2025). This underestimation arises from the low critical densities of [O II] λλ3726,29 ($n_{e,crit} = 10^2$-10^3 cm^{-3}). On the other hand, Y. Zhang et al. (2025) use photoionization models to analyse the impact of varying n_e = 100–20 000 cm^{-3} on the UV and optical line ratios commonly used to determine N/O (e.g. [N II]/[O II]). The study of Y. Zhang et al. (2025) showed that UV emission lines (i.e. N IV] and [N III]) are less sensitive to density changes than optical lines, while that high density models predict higher values of [N II]/[O II] with a difference of 0.2 dex. While our CLASSY sample includes only a few objects at high density, a larger sample of galaxies with densities derived from both [O II] and [S II] would provide more information into the relationship between N/O and n_e at $\log(n_e/\mathrm{cm}^{-3}) > 2.5$.

Overall, our results indicate that n_e play an important role in shaping N/O, potentially contributing to part of the scatter observed in Fig. 2. Since O^+ contributes to the total gas metallicity, it is also important to understand the bias introduced at high densities (e.g. H. Yanagisawa et al. 2024b; Z. Martinez et al. 2025). The impact of density on metallicity estimates has also been noted in other works, for example M. J. Hayes et al. (2025) shows, for a sample of stacked spectra of $z \sim 4-10$ galaxies, that the assumption of very high density gas (10^6 cm^{-3}) to infer T_e[O III] based on the [O III]λ5007/ λ1666 ratio can lead to lower T_e values that align with those in local galaxies. In those high density environments, [O III]λ5007 is collisionally de-excited due to its critical density ($n_{e_{crit}} \sim 10^5$ cm^{-3}), resulting in a reduction of the inferred T_e[O III], which impacts the metallicity by shifting it to higher O/H values. Therefore, the assumption of high density increases the derived metallicity and decreases N/O; in this case, the elevated N/O values seen in some SFGs at high redshift might at least in part be explained by incorrect density assumptions (Z. Martinez et al. 2025). Note that the N/O derived in M. J. Hayes et al. (2025) is based on UV N lines, which are less sensitive to density variations (e.g. R. Marques-Chaves et al. 2024; Y. Zhang et al. 2025).

On the other hand, some studies have analysed the redshift evolution of n_e[S II] (e.g. R. L. Sanders et al. 2016; Y. Isobe et al. 2023; M. W. Topping et al. 2025) finding densities higher than those typical local SFGs. Recently, M. W. Topping et al. (2025) use a sample of galaxies from the AURORA survey (A. E. Shapley et al. 2025), finding a correlation between n_e[S II] and redshift in galaxies at $z = 2-6$ with average values between 300 cm^{-3} and 500 cm^{-3}, similar to the values reported for CLASSY galaxies (D. A. Berg et al. 2022; M. Mingozzi et al. 2022; K. Z. Arellano-Córdova et al. 2024). Our analysis with CLASSY also suggests that high density gas are associated with an enhancement of N/O, independent of the metallicity of the gas (e.g. H. Yanagisawa et al. 2024b; S. R. Flury et al. 2025a).

5.2 The impact of $M_\star$ and SFR on N/O

The relation between N/O with stellar mass has previously been studied using samples of local and high-z galaxies (e.g. E. Pérez-Montero & T. Contini 2009; R. O. Amorín et al. 2010; B. H. Andrews & P. Martini 2013; E. Pérez-Montero et al. 2013; A. L. Strom et al. 2017; C. Hayden-Pawson et al. 2022). In E. Pérez-Montero & T. Contini (2009), these authors show that more massive galaxies implied high N/O abundance than the lower counterpart

because of the rapid chemical evolution of a more massive system. C. Hayden-Pawson et al. (2022) show that $z \sim 2$ galaxies are systematically 0.35 dex shifted to lower N/O in comparison with local galaxies. In contrast, other studies predicted a shift to elevated N/O at higher redshifts (e.g. D. Masters, A. Faisst & P. Capak 2016). However, note such studies are based on the use of strong-line methods in both local and higher redshift observations.

In Fig. 5, we show that the variations in N/O are across stellar masses for CLASSY with large scatter. To analyse the redshift evolution of the N/O and stellar mass plane, we have added the sample of high$-z$ galaxies that we have gathered from the literature. We found that the $z = 2 - 6$ sample, whose N/O derived by optical lines is in good agreement with CLASSY ($z \sim 0$) showing no apparent evolution for a fixed stellar mass up to $z \sim 6$. However, $z > 6$ galaxies (UV N) depart significantly from the bulk of the sample for a fixed stellar mass. For N/H, we get similar results when we include $z = 2 - 6$ galaxies. In general, when we compare the N/H-$M_\star$ plane, our results do not indicate a redshift evolution.

To understate what is causing the dispersion on the N/O -$M_\star$ (see the top panel of Fig. 5), we compare such a relation in colour-coded with n_e[S II] in Fig. 8. Overall, we find that the high density galaxies are clearly causing the scatter for a fixed stellar mass. In addition, we have incorporated the same chemical evolution models as in Fig. 2, but as a function of stellar mass in Fig. 8, illustrating different SFE. For comparison, we also show the models used by C. Hayden-Pawson et al. (2022) in their study of N/O at $z \sim 2$. The chemical evolution models presented in C. Hayden-Pawson et al. (2022) assume a E. E. Salpeter (1955) IMF, a higher infall mass of log(Minf/M$\odot$) $= 12$, and a SFE of $\nu = 5\,\mathrm{Gyr}^{-1}$ and $\tau_{\rm inf} = 7$ Gyr (see also F. Vincenzo et al. 2016). While most of the CLASSY galaxies lie within the parameter space for a fixed stellar mass, high density galaxies deviate from the region traced by the models. Notably, galaxies at $z = 2 - 6$ also align with the set of chemical evolution models presented here, in contrast to the selected models from C. Hayden-Pawson et al. (2022) that include high time infall ($\tau_{\rm inf} = 7$ Gyr) and log($M_{\rm infall}$/M$\odot$) $= 12$, which were used to cover their sample of $z \sim 2$ galaxies. Overall, our results confirm that N/O increases with stellar mass in more evolved galaxies (high $M_\star$) (e.g. E. Pérez-Montero et al. 2013), but also shows a significant scatter associated with high density gas at fixed stellar mass.

Another essential property in the context of galaxy evolution is star formation, we show in Fig. 5 that N/O increases as SFR increases for values of log(SFR/$M_\odot$yr^{-1}) $\gtrsim 1$. Although high values of N/O cover a wide range of stellar mass, the CLASSY galaxies are more closely correlated with the SFR. Such a result is also in agreement with other galaxies at $z \sim 0$ (small circles). Interestingly, when we include the sample of galaxies at high $z = 2 - 6$ (pentagons), we find that these high$-z$ galaxies also follow the relation for CLASSY ($z \sim 0$) with no apparent redshift evolution. We have also inspected the location of $z > 6$ galaxies (squares). Overall, we find that the comparison between N/O and SFR led to a tight relation with less scatter as the SFR increases. In the bottom panel of Fig. 8, we show the N/O$-$SFR plane in colour-coded with n_e, which shows most of the CLASSY galaxies with (logn_e[S II]/cm^{-3}) > 2.5) are mainly associated with high N/O and high SFGs. In a similar way, high-z galaxies tend to follow a similar dependency with n_e than local galaxies. Our results in Figs 5 and 8 indicate that n_e and high SFR might contribute to the scatter of the N/O–O/H and the stellar mass, and the enhancement of N/O for a fixed metallicity.

Since SFGs at high N/O tend to be very compact (e.g. A. Adamo et al. 2024; D. Schaerer et al. 2024; X. Ji et al. 2025), we also investigated the connection between N/O and both SFR and stellar mass surface densities (see Fig. 6). Overall, our results show a tentative correlation between N/O and $\Sigma_{\rm SFR}$, while no clear correlation is found with $\Sigma_{M_\star}$ (see Section 4.4). Since electron density appears closely linked to high N/O values, we selected the CLASSY galaxies with n_e([S II]) > 300 cm^{-3} and compared them with galaxies at $z = 2 - 6$. In Fig. 9, we compare N/O with $\Sigma_{\rm SFR}$ (left) and $\Sigma_{M_\star}$ (right) for the selected high density CLASSY galaxies, colour-coded by metallicity. We find that, as expected, the CLASSY galaxies cover a lower range of $\Sigma_{\rm SFR}$ and $\Sigma_{M_\star}$, with metallicities spanning $12 + \log(\mathrm{O/H}) = 8.0-8.76$, but they show N/O values similar to those of galaxies at $z = 2 - 6$.

Unfortunately, our comparison sample at $z = 2 - 6$ includes only three galaxies with N/O inferred from optical lines, as their effective radii are often not reported in the original studies. In addition, we also include $z > 6$ galaxies where n_e is determined from UV lines (e.g. C III] or Si III]). Note that $z > 6$ galaxies exhibit SFRs similar to those at lower redshift with comparable chemical abundance patterns (e.g. Ne/O) (e.g. K. Z. Arellano-Córdova et al. 2022b, 2025; T. M. Stanton et al. 2025). As we see in Fig. 9, $z > 6$ galaxies show elevated $\Sigma_{\rm SFR}$ and $\Sigma_{M_\star}$, as seen in other recent studies (e.g. X. Ji et al. 2025). Fig. 9

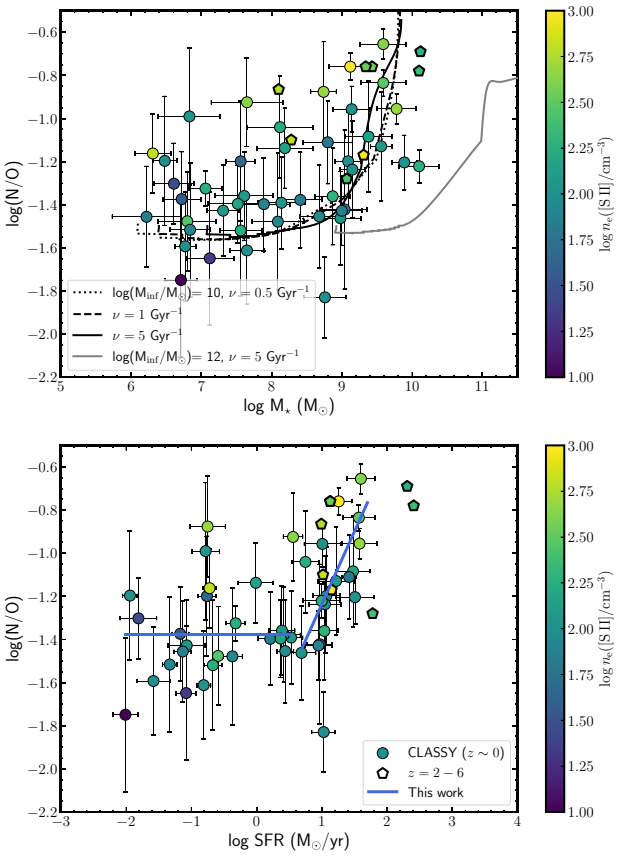

Figure 8. Comparison of N/O as a function of stellar mass (top) and SFR (bottom), colour-coded by n_e[S II]. Part of the dispersion in these relations is due to galaxies exhibiting high density and elevated N/O ratios. Most galaxies at $z = 2$–6 are also located in a similar parameter space in N/O and n_e as those in the CLASSY sample (see also Fig. 4). The different lines represent the chemical evolution models as in Fig. 2, varying only the SFE (ν). For comparison, we also include the chemical evolution models from C. Hayden-Pawson et al. (2022) (grey line), which cover the parameter space of their galaxy sample at $z \sim 2$. The offset in stellar mass is due to higher value in $M_{\rm inf}$ assuming by C. Hayden-Pawson et al. (2022). Note that most of the galaxies at $z = 2$–6 (pentagons) also follow the models presented in this study.

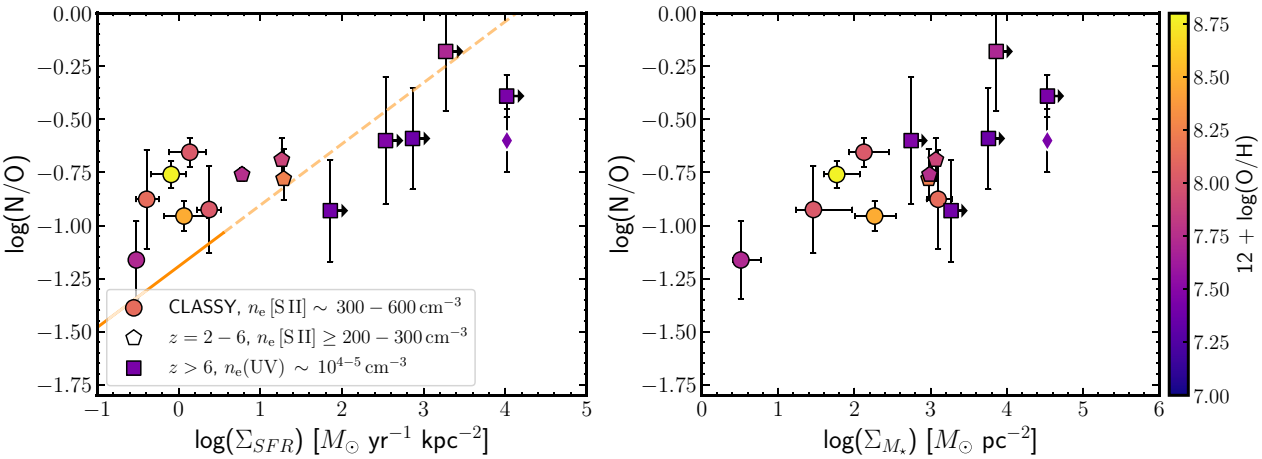

Figure 9. The Σ_{SFR} and $\Sigma_{M_\star}$ as a function of N/O for high-density CLASSY galaxies and high-z galaxies. The right panel shows the ranges in n_e for each sample. The sample of high-redshift galaxies is also included and distinguished according to whether N/O is derived using UV (squares, R. Marques-Chaves et al. 2024; D. Schaerer et al. 2024; M. W. Topping et al. 2024b, a; M. Curti et al. 2025) or optical (pentagons, R. L. Sanders et al. 2023a; Y. Zhang et al. 2025) N lines as in Fig. 2. For RXCJ2248-ID, we have included the N/O ratio derived using optical (diamond symbol) by K. Z. Arellano-Córdova et al. (2025) for comparison with the UV N/O derived in M. W. Topping et al. (2024b). The CLASSY galaxies with high-density values tend to have similar N/O enhancements as galaxies at $z = 2$–6, but exhibit lower SFR and stellar mass surface densities. The combined solid and dashed lines represent an extension of the relation between N/O and Σ_{SFR} derive for CLASSY at $z \sim 0$. Such a relation suggests that N/O increases as the compactness of the galaxy increases.

also shows that galaxies with similar N/O cover different ranges of Σ_{SFR} and $\Sigma_{M_\star}$. For one galaxy at $z \sim 6$, RXCJ2248-ID, it is possible to determine the N/O ratio using only optical lines. K. Z. Arellano-Córdova et al. (2025) inferred the optical N/O ratio of RXCJ2248-ID from the physical conditions and corrected fluxes of [N II] and [O II] reported by M. W. Topping et al. (2024b), reporting a high log(N/O) $= -0.60 \pm 0.15$ compared to the local abundance, which indicates that both UV and optical N lines show a similar degree of enhancement (see also Section 4.3). This value is illustrated in Fig. 9 for comparison (rhomboid). Overall, the CLASSY galaxies with high N/O and high n_e are those with relatively higher metallicity compared to higher-z galaxies. This is consistent with the expectation that, in more evolved galaxies, the contribution of AGB stars enriches the ISM with secondary nitrogen production at 12 + log(O/H) $\gtrsim 8.0$ (e.g. F. Vincenzo et al. 2016). Additionally, our results suggest that part of the dispersion in the N/O–O/H relation (see Fig. 2) might be driven by other properties, such as high log(Σ_{SFR}/M⊙ yr^{-1} kpc^{-2}) > 1 in objects that also have high n_e([S II]) $\gtrsim 300$ cm^{-3} (see Figs 8 and 9). Such a trend might also extend to galaxies at $z = 2 - 6$.

5.3 The impact of stellar feedback on N/O

The baryon cycle is the key link between stellar processes that produce heavy elements in galaxies. In this context, an important component of the baryon cycle is galactic outflows. Our analysis in Fig. 7 indicates that strong outflows correlate with N/O enhancement at $z \sim 0$.

Recent studies of the Sunburst Arc, a galaxy at $z = 2.37$ (12 + log(O/H) $= 7.97$), have revealed interesting physical properties. For example, the analysis of one of its massive clusters shows N/O enhancement likely related to the presence of WR stars (M. Pascale et al. 2023; T. E. Rivera-Thorsen et al. 2024; B. Welch et al. 2025). Our analysis at $z \sim 0$ shows that WR enrichment has a minimal impact on N/O abundances; however, our small sample covers also higher metallicities than the Sunburst Arc. Additionally, R. Mainali et al. (2022) report a strong outflow velocity derived from UV absorption lines ($v_{out} = 350$ km s^{-1}) and n_e([O II]) ~ 300 cm^{-3}, which aligns with the results for galaxies at $z \sim 0$ (see Fig. 7). This suggests that feedback from massive stars also plays an important role in nitrogen enhancement at $z \sim 2$. Another interesting result from this analysis is the anticorrelation between η and outflow velocities (bottom panel in Fig. 7). The expectation from chemical evolution models is that oxygen is preferentially evacuated in outflows relative to other elements (e.g. F. Vincenzo et al. 2016; S. Bhattacharya & C. Kobayashi 2025), which suggests a net positive correlation between η and N/O. This contrasts with what we find in CLASSY. Our results could indicate that nitrogen produced by massive stars is in fact incorporated into outflows (e.g. F. Rizzuti et al. 2025). This effect might be due to the fact that these same massive stars and their surrounding environments are associated with the subsequent CCSNe which drive outflows. However, because the mass threshold for SNe onset may be much lower at lower metallicities (M. C. Jecmen & M. S. Oey 2023), the production and ejection of O as well as the mass loading should be lower in low-metallicity galaxies if SNe are driving the observed outflows. As such, stellar winds may be the key driving mechanism of the observed kinematics. Thus, it seems more likely that the inverse relation between N/O and η is related to N-rich, oxygen poor winds launched by massive stars. While gravitational suppression reduces the outflow launching efficiency, the wind speeds are higher due to line driving (see Section 4.5), which could explain the observed correlation. N-rich winds explain not only the observed correlation with η but also the trend with density. For instance, S. R. Flury et al. (2025b) suggested that 100-200 km s^{-1} winds or outflows could trigger shocks that enhance gas density. They find that their shock scenario is consistent with galactic winds containing N/O excesses of 0.5 dex.

5.4 Chemical evolution models for N and O

By comparing observed abundance patterns with predictions from chemical evolution models, we can place direct constraints on the sources and pathways of enrichment (e.g. F. Vincenzo et al. 2016; D. A. Berg et al. 2019; C. Kobayashi et al. 2020). Here, we investigate the scatter in the N/O–O/H relation by developing new models in the

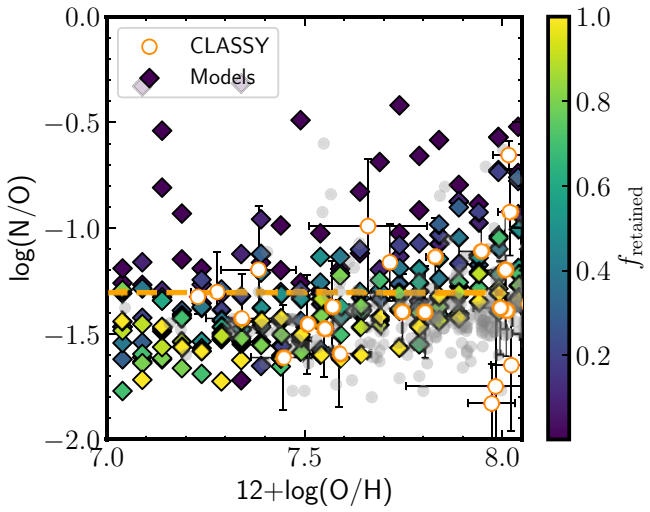

Figure 10. Predicted chemical abundance pattern for a stellar cluster with a total mass of 10^4 $M_\odot$ in the N/O–O/H relation, colour-coded by the retained **explosive** yield fraction ($f_{\rm retained}$). CLASSY galaxies and other local SFGs are included for comparison. The dashed line represents the mean and standard deviation of log(N/O) $=-1.31 \pm 0.23$ for CLASSY galaxies with 12 + log(O/H) < 8.0.

low-metallicity regime (12 + log(O/H) $\lesssim$ 8.0) that consider a simple chemical enrichment scenario. In this regime of low metallicity, the CLASSY galaxies, as well as other dwarf galaxies (small circles) from the literature, show high log(N/O) > −1.25 with respect to the bulk of the observations (see Fig. 2). From our findings in Section 4.5, we show that low-mass galaxies (most of them located in the plateau of the N/O–O/H relation) with high N/O might undergo relatively strong feedback from massive stars.

Our models assume a stellar cluster with a total mass of 10^4 $M_\odot$, adopting the Kroupa IMF (P. Kroupa, C. A. Tout & G. Gilmore 1993). We include rapidly rotating massive stars with initial masses in the range 13-130 $M_\odot$ and adopt the stellar yields from M. Limongi & A. Chieffi (2018) with rotation velocity $v_{\rm rot} = 300$ km/s. In these models, we do not include contributions from AGB stars. Every time a massive star is formed in the IMF sampling, the model updates the cumulative mass of O and N that is ejected in the ISM until a stellar cluster mass of 10^4 $M_\odot$ is formed. A key parameter in these models related to feedback is $f_{\rm retained}$, the fraction of explosive yields retained in ISM from massive stars with $M < 25$ $M_\odot$. We assume that all stellar wind material is fully retained, independent of stellar mass or metallicity, whereas how much is retained from the explosion of stars with $M < 25$ $M_\odot$ is regulated by $f_{\rm retained}$. The selected threshold of $M < 25$ $M_\odot$ is based both on observations of the mass distribution of CCSNe progenitors (e.g. S. J. Smartt 2009; E. O'Connor & C. D. Ott 2011) and on the explodability of massive stars and/or black hole formation from stellar evolution models (e.g. T. Sukhbold et al. 2016).

In Fig. 10, we present the results of our chemical enrichment models in comparison with low metallicity CLASSY galaxies. For these low-metallicity galaxies, we find a mean and standard deviation of log(N/O) $=-1.31 \pm 0.23$ (dashed line), which is slightly elevated compared to our model predictions (coloured diamonds) and the values observed in other dwarf galaxies (small circles). Our models indicate that most CLASSY galaxies are consistent with scenarios where $f_{\rm retained} > 0.6$, suggesting that a significant fraction of the SN ejecta is retained.

However, the CLASSY galaxies exhibiting higher than average N/O ratios may be explained by a more dominant contribution from stellar winds to N enrichment. In Fig. 7, we report relatively strong outflows in low-mass, low-metallicity galaxies compared to galaxies with high stellar masses and metallicities (see also X. Xu et al. 2022). With this correlation in mind, we interpret our model predictions for galaxies with high N/O and low $f_{\rm retained} \sim 0.2$ as indicative of enrichment dominated by stellar winds, with only a small fraction of the explosive ejecta being retained. A follow-up analysis of the N/O abundance patterns in low-mass galaxies is essential to better constrain the role of stellar feedback, including both stellar winds and SNe, in regulating nitrogen enrichment.

6 SUMMARY AND CONCLUSIONS

We investigate the chemical evolution of nitrogen along with oxygen using a sample of 45 local SFGs from the CLASSY survey. This sample includes a broad range of galaxy properties with robust chemical abundance determinations of N and O via the direct-T_e method. We compare the N/O abundance in CLASSY galaxies with their electron density and various properties such as stellar age, stellar mass, SFR, and kinematics (see Section 2). Additionally, we present an analysis of the SFR and stellar mass surface density and their relationship with the N/O ratio across cosmic time. For comparison with our CLASSY findings, we have also included a sample of ($z = 2$–10) galaxies where N/O ratios were determined using UV or optical N lines. In this study, we seek to understand the chemical enrichment pathways of N/O at different metallicities, using a well-defined sample that mimics the properties of high-z galaxies. Moreover, we investigate the main physical drivers of the scatter in the N/O–O/H ratio at $z \sim 0$, to guide the interpretation of high-redshift galaxies observed with *JWST* or other current and future facilities. Our main conclusions from this study are as follows:

(1) We present the N/O–O/H relation for the CLASSY survey, covering a wide range of metallicity values (12 + log(O/H) = 7-9). We find that the N/O abundance ratios align with the expected trend observed in other dwarf galaxies and H II regions at both low and high metallicities, though with some scatter. Particularly, CLASSY show more a constant behaviour for a fixed metallicity.

(2) We found that $z = 2$–6 galaxies exhibit the same correlation and dispersion in N/O–O/H as CLASSY galaxies and other systems at $z = 0$. This similarity suggests that chemical enrichment and evolution pathways do not change with redshift. I.e., comparison of high redshift with CLASSY galaxies indicates not only shared chemical enrichment patterns but also a complete lack of redshift evolution in the production of N relative to O.

(3) We report a significant correlation between n_e([S II]) and the N/O ratio (see Fig. 4). SFGs with log(n_e/cm^{-3}) > 2.5 tend to have elevated log(N/O) ~ -1.0 (see Fig. 4). This result is consistent with findings from galaxies at $z = 2$–6, where elevated N/O persists in high-density environments (e.g. N. A. Reddy et al. 2023a; T. M. Stanton et al. 2025). These results suggest that density structure may significantly contribute to the scatter in the N/O–O/H relation. Therefore, follow-up analyses using galaxy samples with robust density diagnostics are needed to assess the impact of the density structure on the N/O ratio (e.g. D. A. Berg et al. 2021; J. E. Méndez-Delgado et al. 2023a; M. J. Hayes et al. 2025; Y. Zhang et al. 2025; Z. Martinez et al. 2025).

(4) Our comparison between N/O and the global properties of CLASSY galaxies shows that SFGs with log(SFR/M$\odot$ yr^{-1}) > 1

have elevated log(N/O) > -1.2 compared to galaxies with lower SFR. Additionally, galaxies with high SFR also exhibit high n_e([S II]) (see Fig. 8). Interestingly, we find large scatter in N/O as a function of stellar mass, although the correlation is weak. To investigate the origin of this dispersion, our analysis suggests that the density structure contributes, at least in part, to the scatter at fixed $M_\star$. Notably, $z = 2$–6 galaxies occupy a similar parameter space to that implied by CLASSY galaxies at $z \sim 0$ with no apparent redshift evolution.

(5) We investigate whether the chemical enrichment of N/O correlates with stellar mass and SFR surface density. We find a moderate correlation between compactness and high N/O, but no clear correlation with stellar mass surface density at $z \sim 0$. Since Σ_{SFR} tends to correlate with n_e, we compare CLASSY galaxies with high n_e([S II]) to high-z galaxies. We find that galaxies at $z = 2$–6 show similar N/O values but with more compact star formation, which may be consistent with our finding of no chemical evolution in the N/O–O/H relation. In contrast, galaxies at $z > 6$ with more extreme compact star formation are metal-poor, suggesting that, in addition to compactness, other physical mechanisms may play an important role in driving the extreme N/O ratios.

(6) From the analysis of N/O and gas kinematics from UV absorption lines, we find that high-velocity outflows (>100 km s^{-1}) are associated with elevated N/O and high n_e. We also find that the mass-loading factor, η, strongly anticorrelates with N/O, indicating that galaxies with higher N/O (and high stellar mass) are associated with weaker feedback by massive stars. We do not find any clear correlation among N/O and Σ_{SFR}, suggesting that compactness is a property that allows feedback to have a bigger impact for chemical enrichment of N/O at $z \sim 0$. However, at $z \sim 3$, galaxies tend to be more compact, and previous studies have shown that compact star formation correlates with higher values of η (derived using emission lines) (e.g. M. Llerena et al. 2023), in contrast to what we observe in the CLASSY sample. These differences may suggest changes in the relationship between outflows and chemical enrichment. However, X. Xu et al. (2025) show that the mass-loading factor derived from UV absorption lines is systematically larger than the η derived from emission lines.

The results presented here show that high n_e[S II], high SFR, high outflow velocities, and reduced feedback relative to the stellar populations together play a crucial role in shaping the observed N/O values. Interestingly, galaxies at $z = 2$–6 follow the local trend seen in CLASSY, showing no apparent redshift evolution. Larger samples at high z with diverse density diagnostics are essential to improve our understanding of the interplay of all these physical properties in setting N/O levels within galaxies at $z \sim 0$. The scatter in the N/O–O/H relation may reflect a combination of density, SF, and outflows tracing different gas conditions. These findings highlight the need for joint constraints on feedback, chemical abundances, and ISM conditions to understand the chemical evolution of nitrogen in galaxies across cosmic time. A follow-up analysis requires a sample of galaxies with high-resolution UV and optical spectra to connect gas outflow properties across different kinematic components with their chemical enrichment.

ACKNOWLEDGEMENTS

The CLASSY team thanks to our referee Igor Zinchenko for thoughtful feedback that improved this paper. KZA-C and DAB are grateful for the support for this program, HST-GO-15840, that was provided by NASA through a grant from the Space Telescope Science Institute, which is operated by the Associations of Universities for Research in Astronomy, Incorporated, under NASA contract NAS5-26555. The CLASSY collaboration extends special gratitude to the Lorentz Center for useful discussions during the 'Characterizing Galaxies with Spectroscopy with a view for JWST' 2017 workshop that led to the formation of the CLASSY collaboration and survey. The CLASSY collaboration thanks the COS team for all their assistance and advice in the reduction of the COS data.

KZA-C and FC acknowledge support from a UKRI Frontier Research Guarantee Grant (PI Cullen; grant reference: EP/X021025/1). MGS acknowledges support from NSF REU grant AST-1757983 (PI: Jogee) funded by the NSF and Department of Defense, and for support from REU mentors KZA-C and DAB. RA acknowledges support of Grant PID2023-147386NB-I00 funded by MICIU/AEI/10.13039/501100011033 and by ERDF/EU, the Severo Ochoa award to the IAA CEX2021-001131-S, and from the grant PID2022-136598NBC32 'Estallidos8'.

MM, BLJ, SH, and NK are thankful for support from the European Space Agency (ESA).

CK acknowledges funding from the UK Science and Technology Facility Council through grant ST/Y001443/1.

This work also uses observations obtained with the Large 11 Binocular Telescope (LBT). The LBT is an international collaboration among institutions in the United States, Italy, and Germany. LBT Corporation partners are The University of Arizona on behalf of the Arizona Board of Regents; Istituto Nazionale di Astrofisica, Italy; LBT Beteiligungsge-sellschaft, Germany, representing the Max-Planck Society, The Leibniz Institute for Astrophysics Potsdam, and Heidelberg University; The Ohio State University, University of 19 Notre Dame, University of Minnesota, and University of Virginia.

Funding for SDSS-III has been provided by the Alfred P. Sloan Foundation, the Participating Institutions, the National Science Foundation, and the U.S. Department of Energy Office of Science.

The SDSS-III web site is http://www.sdss3.org/. SDSS-III is managed by the Astrophysical Research Consortium for the Participating Institutions of the SDSS-III Collaboration including the University of Arizona, the Brazilian Participation Group, Brookhaven National Laboratory, Carnegie Mellon University, University of Florida, the French Participation Group, the German Participation Group, Harvard University, the Instituto de Astrofisica de Canarias, the Michigan State/Notre Dame/JINA Participation Group, Johns Hopkins University, Lawrence Berkeley National Laboratory, Max Planck Institute for Astrophysics, Max Planck Institute for Extraterrestrial Physics, New Mexico State University, New York University, Ohio State University, Pennsylvania State University, University of Portsmouth, Princeton University, the Spanish Participation Group, University of Tokyo, University of Utah, Vanderbilt University, University of Virginia, University of Washington, and Yale University.

This work also uses the services of the ESO Science Archive Facility, observations collected at the European Southern Observatory under ESO programmes 096.B-0690, 0103.B-0531, 0103.D-0705, and 0104.D-0503.

Software: JUPYTER (T. Kluyver et al. 2016), ASTROPY (Astropy Collaboration 2018, 2022), PYNEB (V. Luridiana et al. 2015), MATPLOTLIB (J. D. Hunter 2007), NUMPY (S. van der Walt et al. 2011), SCIPY (P. Virtanen et al. 2020), and TOWRECAN (S. R. Flury 2025).

DATA AVAILABILITY

All data will be shared by the corresponding author upon reasonable request.

REFERENCES

Abazajian K. N. et al., 2009, ApJS, 182, 543
Adamo A. et al., 2024, Nature, 632, 513
Aggarwal K. M., Keenan F. P., 1999, ApJS, 123, 311
Amayo A., Delgado-Inglada G., Stasińska G., 2021, MNRAS, 505, 2361
Amorín R. O. et al., 2024, A&A, 682, L25
Amorín R. O., Pérez-Montero E., Vílchez J. M., 2010, ApJ, 715, L128
Amorín R., Pérez-Montero E., Vílchez J. M., Papaderos P., 2012, ApJ, 749, 185
Andrews B. H., Martini P., 2013, ApJ, 765, 140
Arellano-Córdova K. Z. et al., 2022a, ApJ, 935, 74
Arellano-Córdova K. Z. et al., 2022b, ApJ, 940, L23
Arellano-Córdova K. Z. et al., 2025, MNRAS, 540, 2991
Arellano-Córdova K. Z., Esteban C., García-Rojas J., Méndez-Delgado J. E., 2020, MNRAS, 496, 1051
Arellano-Córdova K. Z. et al., 2024, ApJ, 968, 98 (AC24a)
Arellano-Córdova K. Z., Rodríguez M., 2020, MNRAS, 497, 672
Asplund M., Amarsi A. M., Grevesse N., 2021, A&A, 653, A141
Astropy Collaboration, 2018, AJ, 156, 123
Astropy Collaboration, 2022, ApJ, 935, 167
Berg D. A. et al., 2012, ApJ, 754, 98
Berg D. A. et al., 2022, ApJS, 261, 31
Berg D. A., Chisholm J., Erb D. K., Skillman E. D., Pogge R. W., Olivier G. M., 2021, ApJ, 922, 170
Berg D. A., Erb D. K., Henry R. B. C., Skillman E. D., McQuinn K. B. W., 2019, ApJ, 874, 93
Berg D. A., Pogge R. W., Skillman E. D., Croxall K., Moustakas J., Rogers N. S. J., Sun J., 2020, ApJ, 893, 96
Berg D. A., Skillman E. D., Henry R. B. C., Erb D. K., Carigi L., 2016, ApJ, 827, 126
Bhattacharya S., Kobayashi C., 2025, preprint (arXiv:2508.11998)
Boggs P. T., Donaldson J. R., Byrd R. H., Schnabel R. B., 1981, ACM Trans. Math. Software, 15, 348
Bunker A. J. et al., 2023, A&A, 677, A88
Byrne C. M., Stanway E. R., Eldridge J. J., McSwiney L., Townsend O. T., 2022, MNRAS, 512, 5329
Cameron A. J., Katz H., Rey M. P., Saxena A., 2023, MNRAS, 523, 3516
Cardelli J. A., Clayton G. C., Mathis J. S., 1989, ApJ, 345, 245
Castellano M. et al., 2024, ApJ, 972, 143
Chabrier G., 2003, PASP, 115, 763
Charbonnel C., Schaerer D., Prantzos N., Ramírez-Galeano L., Fragos T., Kuruvanthodi A., Marques-Chaves R., Gieles M., 2023, A&A, 673, L7
Chisholm J., Rigby J. R., Bayliss M., Berg D. A., Dahle H., Gladders M., Sharon K., 2019, ApJ, 882, 182
Chisholm J., Tremonti C. A., Leitherer C., Chen Y., 2017, MNRAS, 469, 4831
Chisholm J., Tremonti C., Leitherer C., 2018, MNRAS, 481, 1690
Cid Fernandes R., Mateus A., Sodré L., Stasińska G., Gomes J. M., 2005, MNRAS, 358, 363
Croxall K. V., Pogge R. W., Berg D. A., Skillman E. D., Moustakas J., 2016, ApJ, 830, 4
Curti M. et al., 2025, A&A, 697, A89
Edmunds M. G., 2001, MNRAS, 328, 223
Erb D. K., 2015, Nature, 523, 169
Esteban C., Bresolin F., García-Rojas J., Toribio San Cipriano L., 2020, MNRAS, 491, 2137
Florido E., Zurita A., Pérez-Montero E., 2022, MNRAS, 513, 2006
Flury S. R., 2025, towrecan: Quantifying Dispersion in Data. Available at: https://github.com/sflury/towrecan(March 2025)
Flury S. R. et al., 2025a, ApJ, 985, 128
Flury S. R., Arellano-Córdova K. Z., Moran E. C., Einsig A., 2025b, MNRAS, 543, 3367
Flury S. R., Moran E. C., 2020, MNRAS, 496, 2191
Flury S. R., Moran E. C., Eleazer M., 2023, MNRAS, 525, 4231
Froese Fischer C., Tachiev G., 2004, At. Data Nucl. Data Tables, 87, 1
Garnett D. R., 1992, AJ, 103, 1330
Grieve M. F. R., Ramsbottom C. A., Hudson C. E., Keenan F. P., 2014, ApJ, 780, 110
Guo Y. et al., 2016, ApJ, 833, 37
Hayden-Pawson C. et al., 2022, MNRAS, 512, 2867
Hayes M. J., Saldana-Lopez A., Citro A., James B. L., Mingozzi M., Scarlata C., Martinez Z., Berg D. A., 2025, ApJ, 982, 14
Hayes M. J., Scarlata C., 2023, ApJ, 954, L14
Heckman T. M. et al., 2011, ApJ, 730, 5
Heckman T. M., Alexandroff R. M., Borthakur S., Overzier R., Leitherer C., 2015, ApJ, 809, 147
Henry R. B. C., Edmunds M. G., Köppen J., 2000, ApJ, 541, 660
Henry R. B. C., Nava A., Prochaska J. X., 2006, ApJ, 647, 984
Hernandez S., Aloisi A., James B. L., Ferland G. J., Fox A. J., Tosi M., Tumlinson J., 2020, ApJ, 892, 19
Hogarth L. et al., 2020, MNRAS, 494, 3541
Hunter J. D., 2007, Comput. Sci. Eng., 9, 90
Isobe Y., Ouchi M., Nakajima K., Harikane Y., Ono Y., Xu Y., Zhang Y., Umeda H., 2023, ApJ, 956, 139
Izotov Y. I., Guseva N. G., Fricke K. J., Henkel C., Schaerer D., 2017, MNRAS, 467, 4118
Izotov Y. I., Stasińska G., Meynet G., Guseva N. G., Thuan T. X., 2006, A&A, 448, 955
Izotov Y. I., Thuan T. X., 2007, ApJ, 665, 1115
Izotov Y. I., Thuan T. X., Guseva N. G., 2021, MNRAS, 508, 2556
James B. L. et al., 2022, ApJS, 262, 37
James B. L., Koposov S., Stark D. P., Belokurov V., Pettini M., Olszewski E. W., 2015, MNRAS, 448, 2687
James B. L., Tsamis Y. G., Barlow M. J., Westmoquette M. S., Walsh J. R., Cuisinier F., Exter K. M., 2009, MNRAS, 398, 2
Jecmen M. C., Oey M. S., 2023, ApJ, 958, 149
Ji X., Belokurov V., Maiolino R., Monty S., Isobe Y., Kravtsov A., McClymont W., Übler H., 2025, preprint (arXiv:2505.12505)
Johnson J. W., Weinberg D. H., Vincenzo F., Bird J. C., Griffith E. J., 2023, MNRAS, 520, 782
Jones T. et al., 2023, ApJ, 951, L17
Juan de Dios L., Rodríguez M., 2017, MNRAS, 469, 1036
Kisielius R., Storey P. J., Ferland G. J., Keenan F. P., 2009, MNRAS, 397, 903
Kluyver T. et al., 2016, in Loizides F., Schmidt B., eds, Positioning and Power in Academic Publishing: Players, Agents and Agendas. IOS Press, Amsterdam, Netherlands, p. 87
Kobayashi C., Ferrara A., 2024, ApJ, 962, L6
Kobayashi C., Karakas A. I., Lugaro M., 2020, ApJ, 900, 179
Kobayashi C., Karakas A. I., Umeda H., 2011, MNRAS, 414, 3231
Komarova L. et al., 2025, preprint (arXiv:2506.19623)
Köppen J., Hensler G., 2005, A&A, 434, 531
Kroupa P., Tout C. A., Gilmore G., 1993, MNRAS, 262, 545
Kumari N., James B. L., Irwin M. J., Amorín R., Pérez-Montero E., 2018, MNRAS, 476, 3793
Larsen T. I., Sommer-Larsen J., Pagel B. E. J., 2001, MNRAS, 323, 555
Leitherer C. et al., 1999, ApJS, 123, 3
Leitherer C., Ekström S., Meynet G., Schaerer D., Agienko K. B., Levesque E. M., 2014, ApJS, 212, 14
Limongi M., Chieffi A., 2018, ApJS, 237, 13
Llerena M. et al., 2023, A&A, 676, A53
Loaiza-Agudelo M., Overzier R. A., Heckman T. M., 2020, ApJ, 891, 19
Luridiana V., Morisset C., Shaw R. A., 2015, A&A, 573, A42
Mainali R. et al., 2022, ApJ, 940, 160
Maiolino R. et al., 2024, Nature, 627, 59
Marques-Chaves R. et al., 2024, A&A, 681, A30
Martinez Z. et al., 2025, ApJ, preprint (arXiv:2510.21960)
Masters D., Faisst A., Capak P., 2016, ApJ, 828, 18
Matteucci F., Greggio L., 1986, A&A, 154, 279
McClymont W. et al., 2025, MNRAS, 540, 190

McQuinn K. B. W., van Zee L., Skillman E. D., 2019, ApJ, 886, 74
Méndez-Delgado J. E. et al., 2023a, MNRAS, 523, 2952
Méndez-Delgado J. E., Esteban C., García-Rojas J., Kreckel K., Peimbert M., 2023b, Nature, 618, 249
Mingozzi M. et al., 2022, ApJ, 939, 110
Miralles-Caballero D. et al., 2016, A&A, 592, A105
Muratov A. L., Kere vs D., Faucher-Giguère C.-A., Hopkins P. F., Quataert E., Murray N., 2015, MNRAS, 454, 2691
Nakajima K., Ouchi M., Isobe Y., Harikane Y., Zhang Y., Ono Y., Umeda H., Oguri M., 2023, ApJS, 269, 33
Nava A., Casebeer D., Henry R. B. C., Jevremovic D., 2006, ApJ, 645, 1076
O'Connor E., Ott C. D., 2011, ApJ, 730, 70
Osterbrock D. E., 1989, Astrophysics of Gaseous Nebulae and Active GalacticNuclei. University Science Books, Mill Valley, CA
Parker K. S. et al., 2024, ApJ, 977, 104
Pascale M., Dai L., McKee C. F., Tsang B. T. H., 2023, ApJ, 957, 77
Paswan A., Omar A., Jaiswal S., 2019, MNRAS, 482, 3803
Peimbert M., Costero R., 1969, Boletin de los Observatorios Tonantzintla y Tacubaya, 5, 3
Peimbert M., Peimbert A., Delgado-Inglada G., 2017, PASP, 129, 082001
Peng Z. et al., 2025, ApJ, 981, 171
Pérez-Díaz B., Pérez-Montero E., Fernández-Ontiveros J. A., Vílchez J. M., Amorín R., 2024, Nat. Astron., 8, 368
Pérez-Montero E. et al., 2013, A&A, 549, A25
Pérez-Montero E., Contini T., 2009, MNRAS, 398, 949
Podobedova L. I., Kelleher D. E., Wiese W. L., 2009, J. Phys. Chem. Ref. Data, 38, 171
Reddy N. A. et al., 2023a, ApJ, 951, 56
Reddy N. A., Topping M. W., Sanders R. L., Shapley A. E., Brammer G., 2023b, ApJ, 952, 167
Rivera-Thorsen T. E. et al., 2024, A&A, 690, A269
Rizzuti F., Matteucci F., Molaro P., Cescutti G., Maiolino R., 2025, A&A, 697, A96
Rogers N. S. J., Skillman E. D., Pogge R. W., Berg D. A., Croxall K. V., Bartlett J., Arellano-Córdova K. Z., Moustakas J., 2022, ApJ, 939, 44
Rogers N. S. J., Skillman E. D., Pogge R. W., Berg D. A., Moustakas J., Croxall K. V., Sun J., 2021, ApJ, 915, 21
Rogers N. S. J., Strom A. L., Rudie G. C., Trainor R. F., Raptis M., von Raesfeld C., 2024, ApJ, 964, L12
Roy A., Dopita M. A., Krumholz M. R., Kewley L. J., Sutherland R. S., Heger A., 2021, MNRAS, 502, 4359
Salpeter E. E., 1955, ApJ, 121, 161
Sanders R. L. et al., 2021, ApJ, 914, 19
Sanders R. L. et al., 2023a, ApJ, 943, 75
Sanders R. L., Shapley A. E., Kriek M., others, 2016, ApJ, 816, 23
Sanders R. L., Shapley A. E., Topping M. W., Reddy N. A., Brammer G. B., 2023b, ApJ, 955, 54
Scarlata C., Hayes M., Panagia N., Mehta V., Haardt F., Bagley M., 2024, preprint (arXiv:2404.09015)
Schaefer A. L., Tremonti C., Belfiore F., Pace Z., Bershady M. A., Andrews B. H., Drory N., 2020, ApJ, 890, L3
Schaerer D., Marques-Chaves R., Xiao M., Korber D., 2024, A&A, 687, L11
Scholte D. et al., 2025, MNRAS, 540, 1800
Senchyna P., Plat A., Stark D. P., Rudie G. C., Berg D., Charlot S., James B. L., Mingozzi M., 2024, ApJ, 966, 92
Shapley A. E. et al., 2025, ApJ, 980, 242
Smartt S. J., 2009, ARA&A, 47, 63
Stanton T. M. et al., 2025, MNRAS, 537, 1735
Stasinska G., 2023, preprint (arXiv:2312.01873)
Stephenson M. G., Arellano-Córdova K. Z., Berg D. A., Mingozzi M., James B. L., 2023, Res. Notes Am. Astron. Soc., 7, 31
Strom A. L., Rudie G. C., Steidel C. C., Trainor R. F., 2022, ApJ, 925, 116
Strom A. L., Steidel C. C., Rudie G. C., Trainor R. F., Pettini M., Reddy N. A., 2017, ApJ, 836, 164
Sukhbold T., Ertl T., Woosley S. E., Brown J. M., Janka H. T., 2016, ApJ, 821, 38
Tayal S. S., 2011, ApJS, 195, 12
Tayal S. S., Zatsarinny O., 2010, ApJS, 188, 32
Topping M. W. et al., 2025a, ApJ, 980, 225
Topping M. W. et al., 2024b, MNRAS, 529, 3301
Topping M. W. et al., 2025, MNRAS, 541, 1707
Tumlinson J., Peeples M. S., Werk J. K., 2017, ARA&A, 55, 389
van der Walt S., Colbert S. C., Varoquaux G., 2011, Comput. Sci. Eng., 13, 22
Ventura P., Di Criscienzo M., Carini R., D'Antona F., 2013, MNRAS, 431, 3642
Vincenzo F., Belfiore F., Maiolino R., Matteucci F., Ventura P., 2016, MNRAS, 458, 3466
Vink J. S., 2023, A&A, 679, L9
Virtanen P., Gommers R., Oliphant T. E., 2020, Nat. Methods, 17, 261
Watanabe K. et al., 2024, ApJ, 962, 50
Welch B. et al., 2025, ApJ, 980, 33
Xu X. et al., 2022, ApJ, 933, 222
Xu X. et al., 2025, ApJ, 984, 94
Yanagisawa H. et al., 2024a, ApJ, 974, 180
Yanagisawa H. et al., 2024b, ApJ, 974, 266
Zhang Y., Morishita T., Stiavelli M., 2025, preprint (arXiv:2502.04817)

APPENDIX A: GAS AND STELLAR PROPERTIES

A1 Extinction

We have also assessed the impact of gas extinctions and galaxy ages on the N/O–O/H dispersion in Fig. 2. The wavelength separation between the [N II] and [O II] lines makes the [N II]/[O II] ratio more sensitive to extinction corrections. We have compared the $E(B-V)$ values from CLASSY reported in D. A. Berg et al. (2022) to analyse whether the N/O–O/H relation depends on extinction (see also Section 2). Overall, Fig. A1 shows a tentative positive correlation ($\tau = 0.278$ and p-value $= 0.08$). It implies that the N/O ratio tends to increase with extinction. Interestingly, most CLASSY galaxies with high density, $\log(n_e[\mathrm{S\,II}]/\mathrm{cm}^{-3}) > 2.5$, are associated with dustier environments than higher redshift galaxies. This result is in agreement with previous analysis in Lyman continuum emitters where dense gas prevails in regions of high gas extinction (S. R. Flury et al. 2025a).

We have also incorporated a high-z sample with N/O and n_e[S II] for comparison with the CLASSY results. In Fig. A1, we show that high-density objects at $z > 2$ are located below $E(B-V) < 0.2$ with a shift to high N/O compared to galaxies at $z \sim 0$. Recent studies have explored the anomalous discrepancy between the theoretical and observed Balmer ratios based on the assumption of CASE B recombination (e.g. H. Yanagisawa et al. 2024a; W. McClymont et al. 2025; C. Scarlata et al. 2024). Therefore, any failure in dust correction might lead to incorrect values in the determination of N/O, which probably biases our interpretation of Fig. A1. More samples of galaxies at high-z with high-density and N/O are needed to verify its dependency in dustier environments.

A2 EW(Hβ) and stellar age

We have revised the EW(Hβ) as an empirical indicator for intermediate and old ages of the stellar population. EW(Hβ) provides information on the current and previous star formation. Intermediate and old stellar populations do not produce ionizing photons necessary for Hβ emission; however, they can produce and even dominate the underlying continuum. Galaxies with older ages are more evolved, and N/O increases as the new-generation star ejects N into the ISM (e.g. E. Pérez-Montero & T. Contini 2009; F. Vincenzo et al. 2016; J. W. Johnson et al. 2023). Thus, lower EW(Hβ) may provide

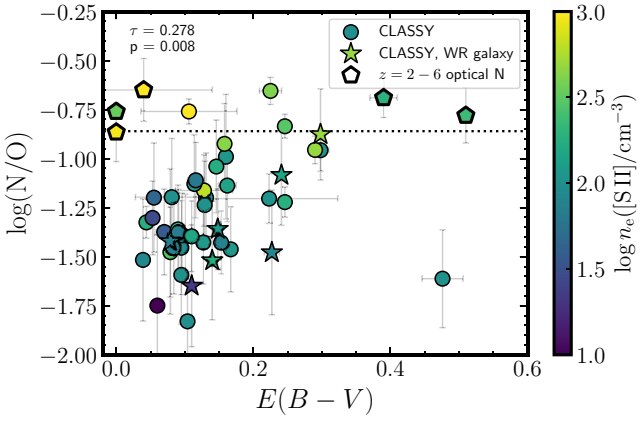

Figure A1. The N/O ratio as a function of the $E(B-V)$ value for CLASSY colour-coded against n_e. There is a tentative positive correlation between N/O and $E(B-V)$, with a dependency with n_e. High-z galaxies are added for comparison showing a shift to high N/O and n_e (R. L. Sanders et al. 2023a; K. Z. Arellano-Córdova et al. 2025; D. Scholte et al. 2025; T. M. Stanton et al. 2025; B. Welch et al. 2025). The $\tau = 0.278$ and p-value $= 0.08$ are also labelled. The dotted line indicates the Solar N/O value. The CLASSY galaxies that host WR stars are marked with a star symbol. The dotted line represents the Solar value of N/O.

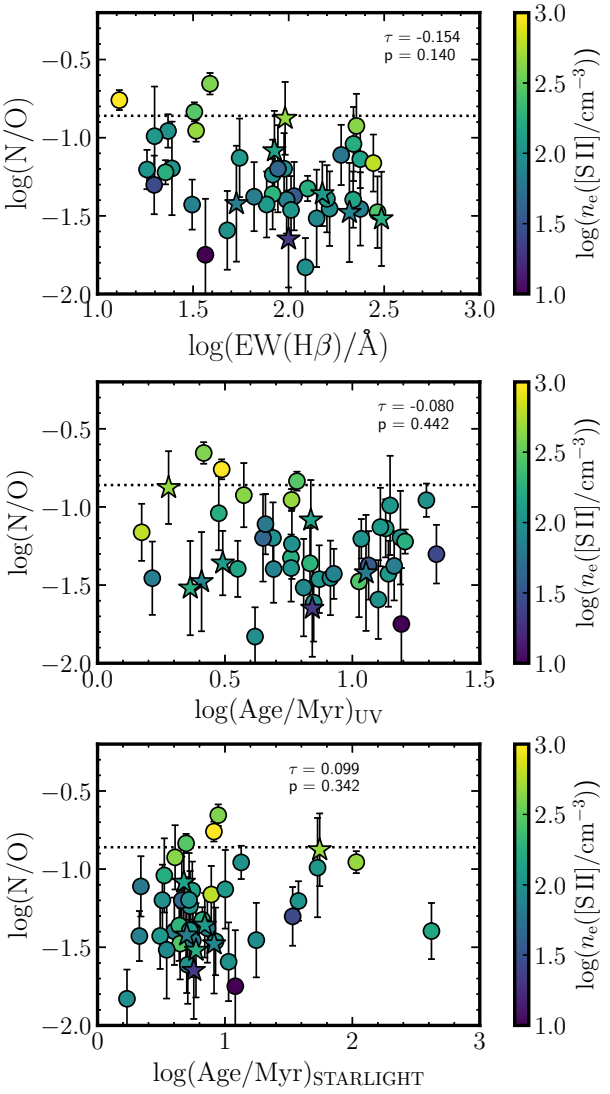

Figure A2. Comparison of EW(Hβ) and stellar age derived from the stellar population fitting from the UV and optical (see also Parker et al., submitted; James et al., submitted) as a function of the N/O ratio for CLASSY and in colour-coded with n_e. There is no statistical correlation between N/O and the EW(Hβ) or stellar age. The dotted lines represent the Solar value of N/O. The star symbols indicate galaxies with WR features.

evidence for contributions from older stellar populations to chemical enrichment. However, using EW(Hβ) purely as an age diagnostic in this context may be misleading given degeneracies between age and stellar mass. Interpreting the EW is further complicated by the fact that, for sufficiently old stellar populations, no ionizing photons are available to produce Hβ emission, meaning that EW(Hβ) traces only populations younger than 10–20 Myr, a time-scale too short to correspond to the AGB stars relevant to nitrogen enrichment.

In the top panel of Fig. A2, we show the relationship between EW(Hβ) and N/O colour-coded with the electron density. For EW(Hβ), we note that the high-N/O is located across all ages with any statistical correlation ($\tau = -0.154$ and $p = 0.140$). Moreover, Fig. A2 also shows that the EW(Hβ)-N/O plane depends on density, indicating that density, not stellar population age, drives the observed N/O abundances (see Section 4.3). In a recent study by M. W. Topping et al. (2025), these authors reported a significant correlation between EW(Hβ) and n_e[S II] using cosmological simulations and observational data from the AURORA Survey (A. E. Shapley et al. 2025). Moreover, M. W. Topping et al. (2025) analysed their results by comparing the log([N II]/Hα) ratio (as representative of metallicity), also finding a trend with EW(Hβ) and n_e[S II]. Such a trend is also observed in Fig. A2 since any metallicity indicator that uses nitrogen lines depends on the N/O abundance.

Following our analysis of EW(Hβ), we have used the stellar ages derived from the results of the best fit to the stellar populations presented in Parker et al., submitted from the UV, which follows the procedure of J. Chisholm et al. (2019) (see also Section 2.3). The middle panel of Fig. A2 presents the analysis of N/O as a function of stellar ages derived from the young stellar population in the CLASSY galaxies. Based on the UV fits, the CLASSY galaxies show UV derived stellar ages ranging from 1 to 30 Myr. In our analysis, we do not find any significant correlation between N/O and UV-based stellar age (Kendall's coefficient of $\tau = -0.080$, p-value $= 0.442$). However, we find that high-gas-density galaxies ($n_e > 300$ cm^{-3}) tend to show higher N/O values and younger ages, as also indicated by the analysis using EW(Hβ). In contrast, galaxies with lower densities ($n_e < 200$ cm^{-3}) exhibit a more constant N/O value for a fixed age. It is important to note that UV observations trace only the youngest stellar populations, while older stellar populations likely contribute significantly to the overall stellar age of the galaxies.

We have also compared the stellar ages derived from stellar population modelling using STARLIGHT (R. Cid Fernandes et al. 2005) applied to the optical spectra from CLASSY (K. Z. Arellano-Córdova et al. 2022a), as derived in James et al. (2025), which may better trace the contributions from older stellar populations to nitrogen abundances. These authors estimate stellar ages by calculating the statistical weights of the stellar light contribution from the best-fitting stellar population models obtained with STARLIGHT. The bottom panel of Fig. A2 shows the comparison between N/O and the stellar ages derived from this optical fitting. For most of the galaxies (approximately 80 per cent), the resulting ages are less than 10 Myr, while a smaller fraction show ages between 10 and

100 Myr. These optical derived ages tend to be higher than those obtained from UV fits and from EW(Hβ) due to the increased contributions of more evolved populations to the optical and the UV. While the youngest stellar populations in the UV are associated with the highest N/O, the light-weighted optical ages are appreciably higher, suggesting an important underlying older population capable of contributing enrichment via AGB stars. Interestingly, one of the WR galaxies, Mrk 996 (also known as J0127−0619), shows an older age (∼50 Myr) compared to other WR galaxies, which is unexpected. It is likely that the stellar age of this galaxy is overestimated due to the complexity of its optical spectrum (see B. L. James et al. 2009).

Overall, Kendall's coefficient ($\tau = 0.099$, p-value $= 0.324$) indicates no significant correlation between N/O and the stellar age derived from the optical fitting. Thus, although different stellar age indicators have their own caveats, we cannot discern a clear impact of stellar age on the N/O–O/H relation. Nevertheless, our results suggest that stellar age might have only a minimal effect on shaping and scattering the N/O–O/H ratio.

APPENDIX B: SOME COMMENTS ON INDIVIDUAL CLASSY GALAXIES

B1 Gas kinematics and n_e from different gas components

Some CLASSY galaxies exhibit different velocity components (narrow and broad) in certain Balmer lines and [O III] λ5007, which can be used to analyse the physical properties of the gas in each component (e.g. L. Hogarth et al. 2020; M. Mingozzi et al. 2022; Z. Peng et al. 2025). For example, L. Hogarth et al. (2020) performed a chemical analysis using high spectral resolution of the compact CLASSY galaxy, J1429+0643, finding high N/O ratios associated with two narrow components ($\log(\mathrm{N/O}) = -0.80 \pm 0.16$ and -1.06 ± 0.11), while the gas in the broad component appears to be more enriched in oxygen ($12 + \log(\mathrm{O/H}) = 8.58$), but shows a typical $\log(\mathrm{N/O})$ of -1.33 ± 0.12 (see Fig. 2). For J1429+0643, we derive $\log(\mathrm{N/O}) = -1.11 \pm 0.19$ using the integrated SDSS profile, consistent within the uncertainties with the N/O values from the narrow components. In terms of n_e, L. Hogarth et al. (2020) derived n_e[S II] = 200–490 cm^{-3}. However, such broad gas components (i.e. velocity dispersion, $\sigma = 240$–1800 km s^{-1}) might be associated with outflows driven by SNe (Y. I. Izotov & T. X. Thuan 2007; L. Hogarth et al. 2020) or by radiation pressure, which becomes more efficient at higher metallicities.

Recently, Z. Peng et al. (2025) studied the physical conditions and metallicities of different kinematic components in 14 CLASSY galaxies. In general, they reported high n_e values across various velocity components (see also Section 4.3), with no significant variations in metallicity, consistent with the findings of L. Hogarth et al. (2020). In our analysis, we are unable to derive abundances for the broad component due to the lack of detection of this component in T_e-sensitive lines or in any lines suitable for determining n_e from [S II]. Nevertheless, this study highlights the importance of understanding the key physical conditions, galaxy properties, and kinematics that influence the determination of gas-phase abundances of nitrogen, and likely other elements. Follow-up analyses using higher resolution spectra of the outflow properties using high-resolution spectra will be essential to disentangle additional chemical enrichment pathways for N/O at $z \sim 0$ (see also Section 5).

[1]*Institute for Astronomy, University of Edinburgh, Royal Observatory, Edinburgh EH9 3HJ, UK*
[2]*Department of Astronomy, The University of Texas at Austin, 2515 Speedway, Stop C1400, Austin, TX 78712, USA*
[3]*AURA for ESA, Space Telescope Science Institute, 3700 San Martin Drive, Baltimore, MD 21218, USA*
[4]*Dipartimento di Fisica e Astronomia 'Ettore Majorana', Università degli Studi di Catania, Via S. Sofia 64, I-95123 Catania, Italy*
[5]*Center for Interdisciplinary Exploration and Research in Astrophysics (CIERA), Northwestern University, 1800 Sherman Ave., Evanston, IL 60201, USA*
[6]*Minnesota Institute for Astrophysics, University of Minnesota, 116 Church Street SE, Minneapolis, MN 55455, USA*
[7]*Instituto de Astrofísica de Andalucía (CSIC), Glorieta de la Astronomía, s.n., E-18080 Granada, Spain*
[8]*LUX, Observatoire de Paris, Universitá PSL, CNRS, 5 place Jules Janssen, F-92190 Meudon, France*
[9]*Department of Physics and Astronomy, Center for Astrophysical Sciences, Johns Hopkins University, Baltimore, MD 21218, USA*
[10]*Department of Astronomy and Oskar Klein Centre for Cosmoparticle Physics, AlbaNova University Centre, Stockholm University, SE-10691 Stockholm, Sweden*
[11]*Centre for Astrophysics Research, Department of Physics, Astronomy and Mathematics, University of Hertfordshire, Hatfield AL10 9AB, UK*
[12]*Department of Physics, University of California, Santa Barbara, Santa Barbara, CA 93106, USA*
[13]*Centre for Astrophysics and Supercomputing, Swinburne University of Technology, PO Box 218, Hawthorn, VIC 3122, Australia*
[14]*The Observatories of the Carnegie Institution for Science, 813 Santa Barbara Street, Pasadena, CA 91101, USA*
[15]*Instituto de Astronomía, Universidad Nacional Autónoma de México, Unidad Académica en Ensenada, Km 103 Carr. Tijuana-Ensenada, Ensenada 22860, México*
[16]*Research School of Astronomy and Astrophysics, Australian National University, Australia*
[17]*ARC Centre of Excellence for All Sky Astrophysics in 3 Dimensions (ASTRO 3D), Australia*
[18]*Center for Astrophysics | Harvard & Smithsonian, 60 Garden Street, Cambridge, MA 02138, USA*

This paper has been typeset from a TEX/LATEX file prepared by the author.